Simultaneous retrieval of $T(p)$ and CO_2 VMR from two-channel non-LTE limb radiances and application to daytime SABER/TIMED measurements

L. Rezac [a,b,*], A. Kutepov [c,d], J.M. Russell III [b], A.G. Feofilov [e], J. Yue [b], R.A. Goldberg [c]

[a] Max Planck Institute for Solar System Research, Göttingen, Germany
[b] Center for Atmospheric Sciences, Hampton University, Hampton, VA, USA
[c] NASA Goddard Space Flight Center, Greenbelt, MD, USA
[d] The Catholic University of America, Washington, DC, USA
[e] Laboratory of Dynamical Meteorology, École Polytechnique, Palaiseau, France

ARTICLE INFO

ABSTRACT

The kinetic temperature, T_k, and carbon dioxide, CO_2 density, are key parameters that characterize the energetics and dynamics of the mesosphere and lower thermosphere (MLT) region. The Sounding of the Atmosphere using Broadband Emission Radiometry (SABER) instrument on-board the Thermosphere-Ionosphere-Mesosphere-Energetics and Dynamics (TIMED) satellite has been providing global, simultaneous measurements of limb radiance in 10 spectral channels continuously since late January 2002. In this paper we (1) present a methodology for a self-consistent simultaneous retrieval of temperature/pressure, $T_k(p)$, and CO_2 volume mixing ratio (VMR) from the broadband infrared limb measurements in the 15 and 4.3 μm channels, and (2) qualitatively describe the first results on the CO_2 VMR and T_k obtained from application of this technique to the SABER 15 and 4.3 μm channels, including issues, which demand additional constraints to be applied.

The self-consistent two-channel retrieval architecture updates parameters at all altitudes simultaneously, and it is built upon iterative switching between two retrieval modules, one for CO_2 and one for T_k. A detailed study of sensitivity, stability and convergence was carried out to validate the algorithm. The T_k/CO_2 VMR distribution can be reliably retrieved without biases connected with this non-linear inverse problem starting with an initial guess as far as $\pm$ 20% of CO_2 VMR and $\pm$ 15 K from the solution (as global shift, or somewhat larger if only local deviations are considered).

In polar summer toward high latitudes the retrieved CO_2 VMR profile shows a local peak around 90 km. We discuss details of this feature and show that: (a) it is not an algorithm artifact or instability, (b) additional a priori constraints are needed in order to obtain a physical profile and to remove this peak, and (c) several possibilities are explored as to uncover the real cause of this feature, but no firm conclusion can be reached at this time.

This algorithm has been applied to all available daytime SABER measurements since 2002, and the first results of the mean CO_2 VMR profiles and their distribution is discussed. In particular, the CO_2 VMR profiles depart from a well mixed value at altitudes of 65–70 km during equinoxes at high and mid-latitudes, but in the summer hemisphere solstice period the SABER data is more consistent with a well mixed VMR conditions extend up to 87–90 km especially toward high latitudes.

© 2015 Elsevier Ltd. All rights reserved.

1. Introduction

Carbon dioxide becomes a dominant greenhouse gas above the tropopause, due to diminishing water vapor opacity (Lindzen, 2007). Its dominant role in the energy budget of Earth's stratosphere, mesosphere and lower thermosphere altitude range about 15–120 km is due to infrared radiative cooling from emissions in the 15 μm bands (Roble and Dickinson, 1989). Investigations of ice core data suggest a steady CO_2 VMR increase over the past 200 years (Oeschger and Siegenthaler, 1987) in the troposphere, going from about 270–280 (ppmv) in ~1800 to about 400 (ppmv) in 2014 (Tans, 2014). This increase has been attributed mainly to anthropogenic activities related to fossil fuel burning and

deforestation. The rising CO_2 levels affect middle and upper atmospheric layers through enhanced cooling and subsequent contraction of the atmosphere (Akmaev, 2002), with a time lag of about 5–6 years due to the time for CO_2 near the surface to propagate to levels in the upper stratosphere (Bischof et al., 1985). Importance of observing and understanding CO_2 concentrations in the MLT region goes beyond the radiative cooling. For example, CO_2 is a long lived tracer influenced by dynamical and mixing processes; hence it is suitable for monitoring the global turbopause height. Below the turbopause, eddy (turbulent) mixing is many times stronger than the molecular diffusion that tends to vertically separate heavier and lighter constituents. Early observations led to a belief that the atmosphere is well mixed up to about 100 km (Trinks and Fricke, 1974; Trinks et al., 1978). However, other measurements of CO_2, including several recent ones, imply a much weaker eddy mixing, suggesting that the turbopause can be as low as 75–80 km (Girard et al., 1988; López-Puertas and Taylor, 1989; Zaragoza et al., 2000; Kaufmann et al., 2002; Beagly et al., 2010). For a detailed review of the physical and dynamical processes establishing the CO_2 VMR profile see review papers (by e.g. López-Puertas et al., 2000; Garcia et al., 2014).

The Sounding of Atmosphere using Broadband Emission Radiometry (SABER) instrument is the first infrared limb emission satellite sensor to complete a full solar cycle of observations in the MLT. Infrared radiances in this region are strongly affected by non-LTE, and therefore development of a multi-channel retrieval algorithm is very challenging. The first simultaneous T_k/CO_2 non-LTE retrieval applied to SABER data was published by Mertens et al. (2003). This algorithm was applied to daytime measurements and yielded SABER version v1.06 dataset. However, because of severe non-linearities, the retrieval algorithm had trouble converging and to avoid further instability, several constraints were imposed. This resulted in over-constrained retrieved CO_2 VMR profiles that were inconsistent from orbit to orbit (B.T. Marshall 2009, private comm.). Hence, in the subsequent SABER data release (v1.07) the T_k retrievals use a CO_2 VMR supplied from averaged day/night profiles of the Whole Atmosphere Community Climate Model (WACCM) model (for more discussion on the difference between v1.06 and v1.07 data processing see Remsberg et al. (2008).

In this paper we describe a newly developed two-channel retrieval of T_k and CO_2 VMR with the goal to overcome the difficulties associated with this non-linear inversion. The non-linearities are associated with (1) optical thickness of the CO_2 line (reaching several 100 for the 4.3 μm at 73 km), (2) due to non-linear way that temperature and volume mixing ratio impacts the non-LTE populations and the limb radiances. Another source of non-linearity is the hydrostatic pressure assumption, which is applied during iterations. These non-linear effects will be discussed later, in particular their effect on the retrievals. The focus is on self-consistency and stability of the algorithm, with well determined statistical uncertainties. The paper is structured as follows: in Section 2 we describe the SABER instrument and the limb measurements in the 4.3 and 15 μm channels, Section 3 contains details on the CO_2 non-LTE model applied and in Section 4 details on the simulation of the broad band limb radiances are presented. In Section 5 we describe the retrieval approach, sensitivity and error analysis of temperature and CO_2 profiles. In Section 6 first results from the self-consistent inversion are presented and in Section 7 results are summarized.

2. SABER instrument and measurements

The SABER instrument was launched on-board the Thermosphere Ionosphere Mesosphere Energetics and Dynamics (TIMED) satellite from Vandenberg Air Force Base on December 7, 2001. It

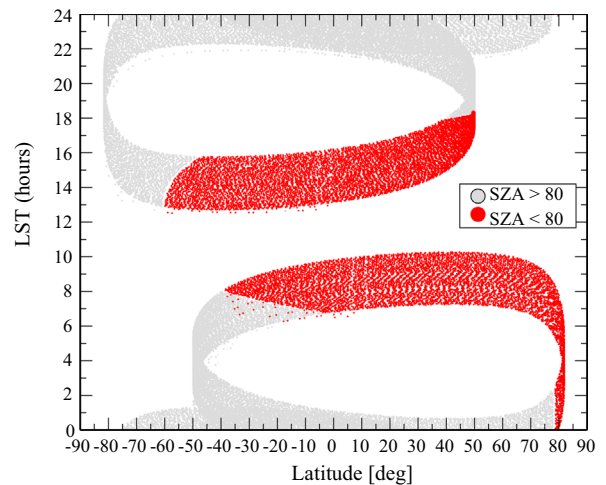**Fig. 1.** Local solar time versus latitude for May 2012. The red dots correspond to conditions SZA <80, which are considered daytime and selected for retrievals, while SZA >80 are colored gray and are not considered for the two-channel inversion in the present work. (For interpretation of the references to color in this figure caption, the reader is referred to the web version of this paper.)

was placed into a nominal circular orbit at 625 km, inclined at 74° with an orbital period of 97 min. SABER measures infrared limb radiance profiles in 10 broad band spectral channels ranging from 1.6 to 17 μm with a vertical sampling of 0.35 km and 2 km field-of-view (FOV). It scans the limb perpendicular to the TIMED velocity vector, and provides nearly global coverage alternating between 83°N–52°S and 83°S–52°N approximately every 60 days. For a complete instrument description, radiometric performance, and calibration see Russell III et al. (1999). In this work the 15 μm narrow channel, Ch1: (606–714 cm^{-1}), is used for retrieval of kinetic temperatures and the 4.3 μm channel, Ch7: (2284–2409 cm^{-1}), for CO_2 VMR retrievals. To ensure high signal-to-noise (S/N) in Ch7 over the entire retrieval grid only daytime measurements are selected for the inversion, using the criterion that the solar zenith angle (SZA) must be less than 80°. In Fig. 1 the local solar time versus latitude for May (2012) is plotted in order to illustrate the daytime data sampling. Two different clusters of local time are sampled at most latitudes (i.e., before noon or after noon), but toward the high latitudes only a single cluster of local time is sampled (before noon). In addition, another data screen is applied based on the Kp index <4 in order to sample only geomagnetically quiet conditions in order to minimize the NO^+ emissions contribution to the SABER Ch7 bandpass radiances at high latitudes (Winick et al., 1987; Picard et al., 1987). In polar summer with long solar illumination periods and NO^+ buildup, model predictions estimate around a 3–5% contribution in Ch7 from the NO^+ emissions at 130 km altitude (Kaufmann et al., 2002; Mertens et al., 2009).

The upper boundary for temperature retrieval is determined mostly due to smaller S/N in Ch1, which is ~5 at 115 km, while Ch7 daytime measured radiances have a S/N of ~45 at 130 km. In the case of Ch7, the upper boundary is limited due to inadequate knowledge of the atmospheric inputs required for the forward modeling, especially the $O(^1D)$ and atomic O VMR. Above the upper boundary (115 km for T_k and 130 km for CO_2), both the temperature and CO_2 VMR are merged with the WACCM profiles used in the SABER operational retrieval in the interval of ± 5 km from the boundary grid point. The retrieval of CO_2 VMR between ~115 and 130 km relies on the WACCM temperature profile, but this does not severely limit the accuracy of the retrieved CO_2 VMR because of non-thermal excitation mechanisms at the emitting levels, as discussed in Section 4. However, the uncertainty of $O(^1D)$

VMR plays significant role on the CO_2 VMR retrieval uncertainty in the 115–130 km region. Similarly, below the 65 km retrieval boundary we smoothly merge the profiles into the SABER operationally retrieved temperature and the WACCM CO_2 VMR.

3. Non-LTE model

The forward model used for simulating the non-LTE limb radiances observed by SABER is divided into two parts: (1) the solution of the non-LTE problem which yields the vibrational populations at each vertical grid point for given atmospheric conditions and (2) the limb radiance calculation module. The solution of the non-LTE problem, that is solving the coupled system of equations of statistical equilibrium and the radiative transfer, is facilitated by the ALI-ARMS (Kutepov et al., 1998; Gusev and Kutepov, 2003; Feofilov and Kutepov, 2012) package based on the Accelerated Lambda Iteration approach (Rybicki and Hummer, 1991). The non-LTE radiative transfer is optimized using the framework of opacity distribution functions (ODF) (Mihalas, 1978; Hubeny and Lanz, 1995), which greatly accelerates the radiative transfer calculation for the 15 and 4.3 μm bands by a factor of ≈ 100–200 (Feofilov and Kutepov, 2012). The ODF method is very accurate especially for linear molecules such as CO_2. The vibrational temperatures compared to those calculated by a line-by-line radiative transfer method are ≤ 1 K for all levels. A total of 56 vibrational levels for the four main CO_2 isotopes and 120 bands are considered in order to properly model the CO_2 populations relevant for SABER non-LTE radiances. In the subsequent discussion we adopt the HITRAN notation (Rothman and et al., 1992) designating the CO_2 vibrational levels as (ν_1, ν_2, ℓ, ν_3, n), where ν_1 is the quantum number designating the symmetric stretch mode [1388 cm^{-1}], ν_2 the bending mode [667 cm^{-1}], ℓ is the quantum number describing the angular momentum, ν_3 is the quantum number for the asymmetric stretch mode [2349 cm^{-1}], and n denotes the Fermi group. The quantities in the brackets refer to the vibrational energy of the given level. Fig. 2 shows a simplified level diagram for the most important radiative transitions in the 15 and 4.3 μm bands used in this work including the solar pumping transitions at 2.0, 2.7 and 4.3 μm. Besides the radiative transitions, there are numerous vibration–translation (V–T) and vibration–

vibration (V–V) energy exchange processes that directly or indirectly influence the vibrational populations of CO_2 that are not depicted in the diagram. However, the rapid exchange of ν_3 quanta through V–V processes between excited N_2 and CO_2 (ν_3) is shown. The V–V exchange of the ν_2 quanta between the (626) isotope and the minor isotopes, which plays an important role especially in polar summer MLT (Kutepov et al., 2006), is also depicted in the diagram. For the isotopes the highest level considered in the non-LTE model is the 10011, similar to the work of López-Puertas et al. (1998) and Kaufmann et al. (2002) (not shown in Fig. 2). The distribution of the isotopic levels is similar to that of the main isotope as shown. The vibrational populations are calculated assuming the rotational sub-levels obey the Boltzmann distribution (rotational LTE). The radiative transfer and the solar absorption are calculated for all lines of all bands available in the HITRAN 2008 (Rothman et al., 2009) catalog with the solar flux at the top-of-atmosphere (TOA) taken from work of Kurucz (1995), which is also used in SABER operational algorithms, and scaled to the Earth–Sun distance for a given day of the year. The radiative transfer equation is numerically solved using the discontinuous finite element (DFE) (Castor et al., 1992) method. The set of all relevant rates describing excitation due to V–T and V–V processes is taken from the work of Shved et al. (1998) and further detailed in Gusev (2002). The quenching of CO_2 (ν_2) by the atomic oxygen collision rate coefficient of 6×10^{-12} cm^3 s^{-1} is used and scaled to given layer temperatures with the general expression $\sqrt{T/300}$. Feofilov et al. (2012) provide detailed discussion on the measurement history of this rate and the current uncertainties for atmospheric science applications. Other important input parameters are $T(p)$, and mixing ratios of CO_2, O, O(^{1}D), N_2 and O_2. These atmospheric variables are taken from the SABER operational retrieval (T_k (p), O, O(^{1}D)) and WACCM model(N_2 and O_2). Above ~110 km all the atmospheric inputs necessary for the non-LTE and limb calculation are taken from the WACCM model, which is supplied in the SABER v2.0 data files. In the case of temperature and CO_2 VMR these profiles represent initial guess and are later retrieved simultaneously. The daytime SABER O VMR profile is operationally retrieved up to 90 km from the 9.6 μm channel (Mlynczak et al., 2013) and merged with the WACCM profile above this altitude. The SABER O(^{1}D) profile is also retrieved below (90–95) km from photochemical considerations relying on the WACCM O_2 and the
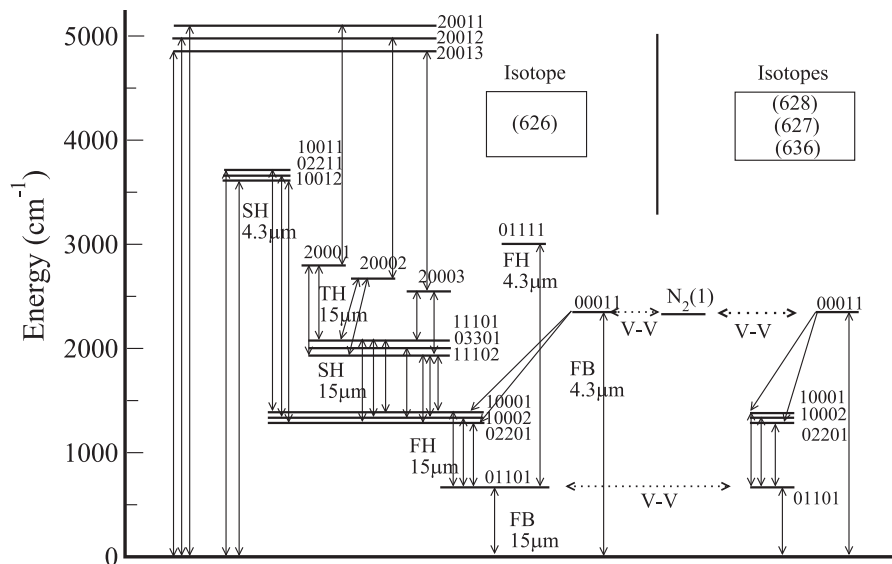

Fig. 2. Simplified CO_2 energy level diagram, showing only subset of the total 56 levels considered. Arrows show the main radiative transitions and dotted arrows depict V–V exchange. FB stands for fundamental band; FH, first hot; SH, second hot and TH, third hot band. The highest vibrational state considered in the non-LTE scheme relevant for SABER measurements is the 20011 level of the main isotope with energy at 5099.66 cm^{-1}.

SABER O_3 retrieved up to 100 km. The SABER $O(^1D)$ is merged with WACCM $O(^1D)$ profile above this height. The WACCM profiles used in the v2.0 SABER data processing are available as a function of space, time, and solar illumination, reflecting the continuous changes in the satellite position for each measurement separately.

4. Ch1 and Ch7 limb radiance calculations

The SABER Ch1 spectral band pass function covers $108 \, cm^{-1}$, and there are a total of 36 bands that are simulated to accurately model the measured limb radiances above the altitude of 65 km. The Ch7 spectral response function covers $125 \, cm^{-1}$ and there is a total of 25 CO_2 bands contributing into the total radiance. The (scaled) SABER response functions for Ch1 and Ch7 along with the CO_2 bands in the corresponding spectral range are shown in Figs. 3 and 4 at the tangent height 100 km for typical polar summer conditions and solar-zenith-angle (SZA)=60°.

Because the retrieval code is applied only to measurements made above 65 km, emissions from molecular species other than CO_2 in the Ch1 and Ch7 channels are negligible. We avoid potential contribution from NO^+ in Ch7 by selection only daytime, geomagnetically quiet conditions, as discussed in Section 2. The only likely contributor is O_3 emissions from the ν_2 band into Ch1 bandpass. We assessed the ozone contribution using a forward model for typical ozone mesospheric concentration, and found <1% additional radiance due to O_3 at 65 km, quickly diminishing to <0.5% at 70 km. In order to retain high forward model accuracy, the limb radiances are calculated with a line-by-line technique accounting for spectral overlap between emission lines within the same band and/or lines of different bands. In order to properly model the narrow Doppler broadened lines in the upper atmosphere, a very fine wavenumber grid is set up that spans the entire band pass of the SABER channel in question. To speed up the limb radiative transfer calculations, a search is first performed going through all lines of all CO_2 molecules to determine the left and right cut-off limits on the wavenumber grid beyond which a particular line does not have to be considered for overlap. These limits are based on the value of line opacity being greater than 1×10^{-5}, which was determined empirically from a number of test runs. This procedure is performed only once for each new retrieval and cuts running time by a factor of 40 while retaining accuracy to better than 0.05% at the lowest tangent heights (65 km). A spherically symmetric atmosphere is assumed in the limb
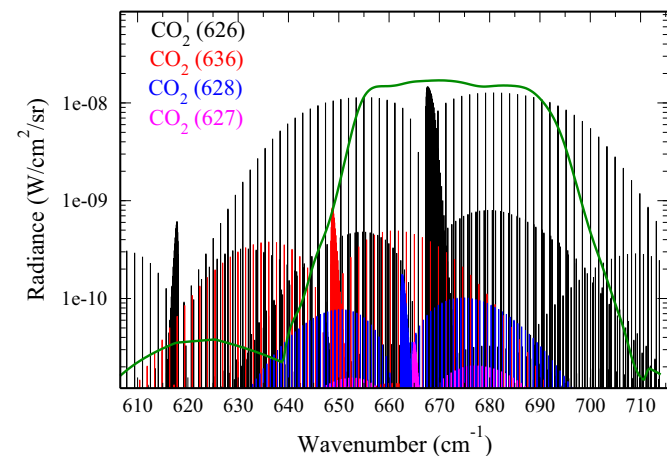

Fig. 4. The 4.3 μm, Ch7, synthetic limb radiances at 100 km with the (scaled) SABER spectral response function over-plotted (dark green). The different colors correspond to the different isotopes as labeled. (For interpretation of the references to color in this figure caption, the reader is referred to the web version of this paper.)
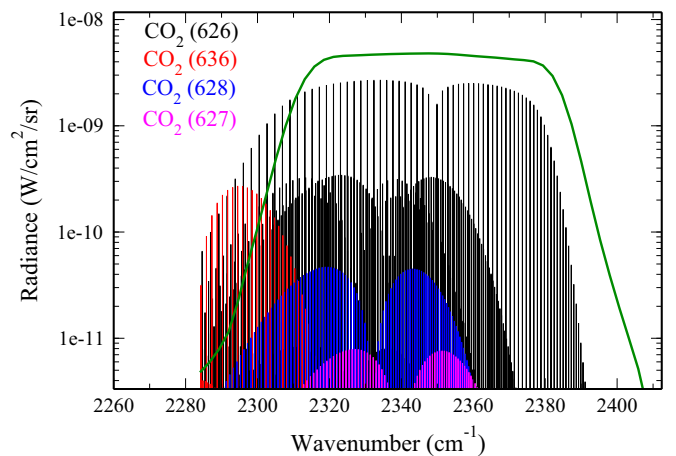
calculations, with each shell having a homogeneous distribution of pressure, temperature and trace gas density. The photon paths along the line-of-sight LOS are modeled without accounting for refraction, which is insignificant for signals at altitudes relevant for this study. We do not explicitly consider effects of horizontal inhomogeneity of atmosphere in the retrievals. They are poorly known in the upper atmosphere and vary in season and latitude. In addition, a rigorous treatment would necessitate such information for all the input atmospheric variables required by the non-LTE forward model. Nevertheless, we estimate their possible effect a posteriori from the retrieved data (i.e., combined effect of horizontal gradients and temporal variability). These are discussed in the summary.

4.1. Ch1 emissions

The daytime 15 μm emissions are generated due to radiative and collisional excitation of the ν_2 manifold levels as well as by radiative and/or collisional decay of the ν_3 manifold pumped by the solar radiation in 2.0, 2.7 and 4.3 μm. Radiative excitation is important up to about 100 km, where collisions with atomic oxygen start dominating the excitation mechanism and spontaneous emission dominates the de-population mechanism. The thermal structure itself plays a significant role in determining vibrational populations of the ν_2 level, up to the lower thermosphere, 100–110 km, especially for the fundamental band, FB, (01101–00001), of the main CO_2 isotope. Under polar summer conditions with very cold temperatures in the mesosphere and a warm upper stratosphere the optically thin FB of the minor isotopes (636, 628, 627) efficiently absorb the up-welling radiation from the warm stratosphere and through very fast V–V exchange, the ν_2 quanta is transferred to the (626) FB level (Kutepov et al., 2006). Detailed description of all individual excitation processes for the ν_2 level can be found in a number of papers including Edwards et al. (1993), López-Puertas et al. (1992) and López-Puertas and Taylor (2001). The most important radiance contributor to Ch1 comes from the transition (01101–00001) of the (626) CO_2 isotope, i.e., the fundamental band. It is only in the altitude range 65–85 km, with maximum at 80 km that the FB of the minor isotopes and first hot (FH) band of the 626 significantly compete with the radiance contribution of the FB of the main isotope, as shown in Fig. 5. The fractional LOS contribution shown in panel (b) Fig. 5 depends on particular atmospheric conditions; nevertheless, this picture is a valid representation of the general

Fig. 3. The 15 μm, Ch1, synthetic limb radiances at 100 km with the (scaled) SABER spectral response function over-plotted (dark green). The different colors correspond to the different isotopes as labeled. (For interpretation of the references to color in this figure caption, the reader is referred to the web version of this paper.)
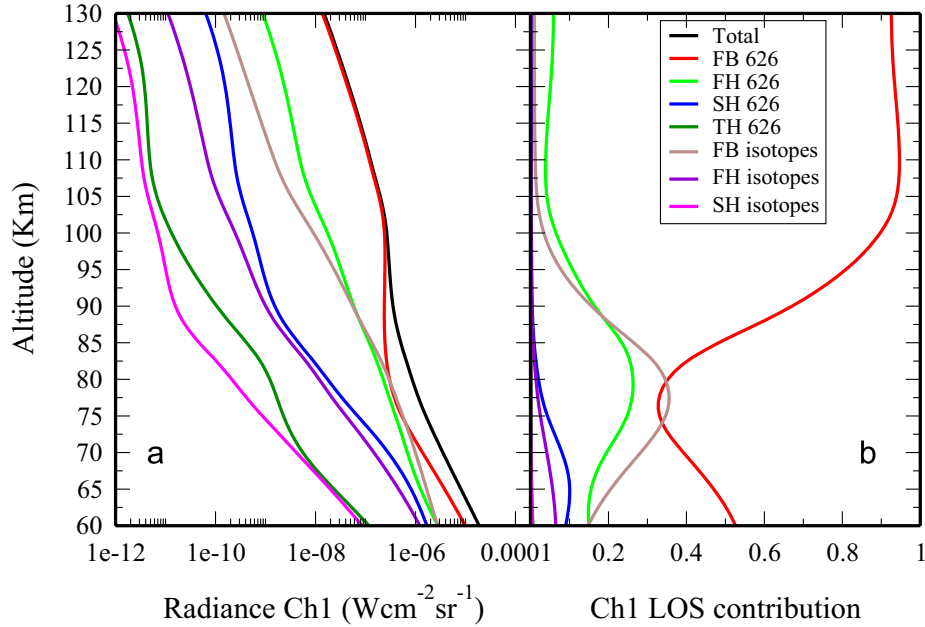
Fig. 5. Panel (a) shows the simulated limb radiances for the most important bands, and in panel (b) the fractional contribution of the CO_2 bands to the total LOS radiance is shown. Calculations are performed for a typical mid-latitude daytime atmosphere assuming SZA=60. FB stands for fundamental band; FH, first hot; SH, second hot and TH, third hot band. The FB, FH, and SH for isotopic bands represent a sum for the 636, 628, 627 CO_2 isotopes.

behavior. The limb radiance of the 626 FB is optically thick up to tangent heights of about 100–105 km, which means that radiances for lower tangent heights may receive non-negligible contributions from higher altitudes. Even radiances at a tangent height of 80 km may have non-negligible contributions from thermospheric layers, which is reflected in the radiance contribution functions shown in Fig. 6. The contribution functions are calculated as a ratio of radiance originating from individual path segments along the LOS to the total LOS radiance at a given tangent height.

4.2. Ch7 emission

In the daytime the primary excitation mechanism for the ν_3 levels is absorption of solar radiation. For this reason the observed intensity varies strongly with the SZA (Shved et al., 1998; López-Puertas and Taylor, 2001). However, at altitudes below 80 km, the ν_3 populations become part of a complex scheme of energy exchanges involving near resonant V–V exchange with N_2. The N_2

Fig. 6. Normalized Ch1 limb contribution functions for selected tangent altitudes. The calculations are performed on a 1 km vertical grid, however, only every 5th contribution function is shown for clarity. The calculations were performed for conditions of a mid-latitude daytime atmosphere, SZA=60. See text for details.

molecule itself channels some of the energy originating from the photo-dissociation of O_2 and O_3 because it is very efficient at de-activating $O(^1D)$ resulting in N_2 vibrational excitation. This process also significantly influences CO_2 populations in the altitude range of 105–115 km since the SH bands become weaker as discussed later. In addition the atmosphere is optically thick at 4.3 μm at the altitudes around 70–75 km and the energy entering through the system, $O(^1D) \rightarrow N_2 \leftrightarrow CO_2(\nu_3) \leftrightarrow \Delta E$ (where the ΔE argument symbolizes a 4.3 μm photon and the arrows symbolize direction of the energy transfer) may be scattered multiple times coupling these altitudes (70–75 and 105–115 km) together. Because of this, the non-LTE radiative transfer at 4.3 μm becomes complicated (Harris and Adams, 1983; Shved et al., 1998), and so does the retrieval. Another important process influencing the reservoir of the ν_3 quanta in the altitude range 60–80 km is the splitting of ν_3 quanta into ν_2 quanta. The most important collisional partners in this V–T process are N_2 and O_2.

In general, there is very little direct dependence of the ν_3 populations on the T_k profile itself which is in contrast to the ν_2 vibrational manifold behavior. This is due to the daytime excitation of the ν_3 levels being driven by solar radiation at 4.3, 2.7, and 2.0 μm. The FB (00011) and FH (01111) bands of the 626 isotope are mainly populated by the absorption of 4.3 μm solar radiation affecting altitudes above 90 km. The more deeply penetrating 2.7 μm radiation will influence CO_2 populations at altitudes below 90 km. The relative band contribution into Ch7, including those of the isotopes, is shown in Fig. 7. Above 105 km the 626 FB makes up more than 90% of the total Ch7 radiance. At altitudes between 87 and 93 km, the FB and second hot (SH) bands of the main isotope contributions are comparable, but the SH bands contribute the most between 70 and 87 km. Below 70 km, the contributions enter a transition region where the most important contributions move again from SH to FB of the main isotope. However, unlike the optically thick 636 FB, the weaker isotopic FB bands (627, 628) also contribute noticeably at these altitudes. An exhaustive description of the ν_3 vibrational levels excitations for both day and night can be found in Shved et al. (1998), López-Puertas and Taylor (1989), and López-Puertas et al. (1998).

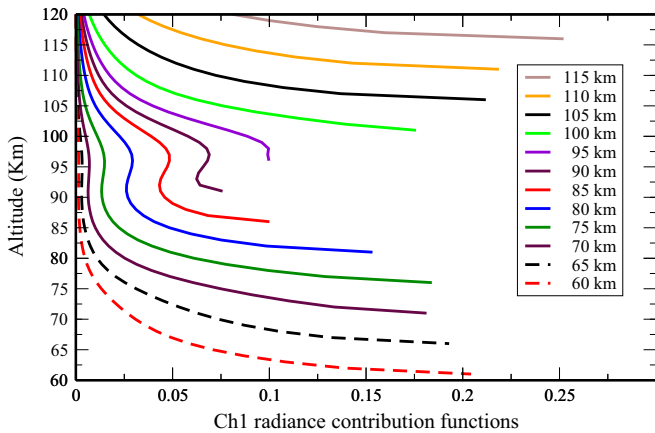Fig. 8 shows the radiance contribution functions for Ch7. The
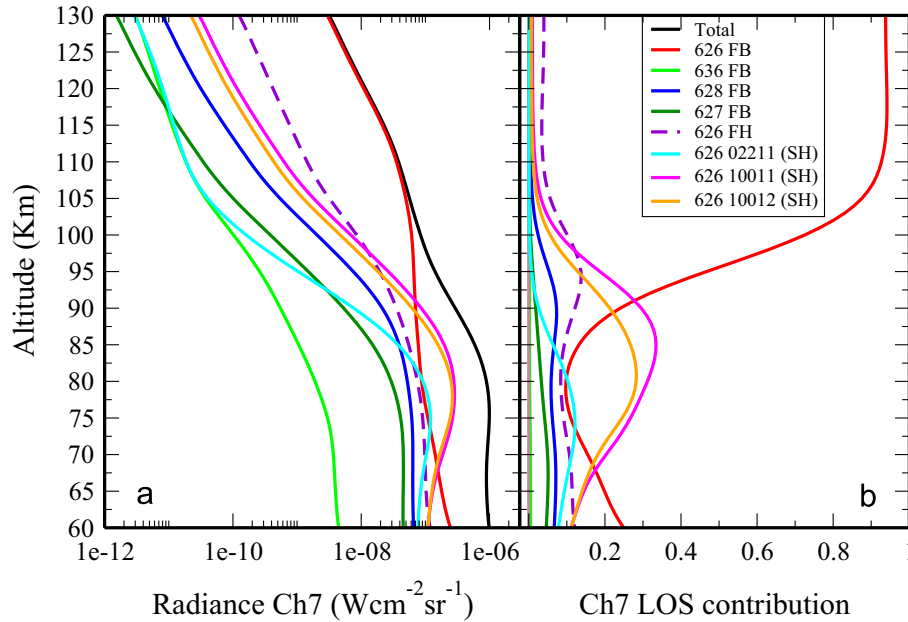
Fig. 7. Panel (a) shows the simulated limb radiances for the most important 4.3 μm bands. Panel (b) shows the fractional contribution of the CO_2 bands to the total LOS radiance. Calculations are performed for a typical mid-latitude daytime atmosphere, SZA=60.

Fig. 8. Normalized Ch7 limb contribution functions for selected tangent heights. The calculations are performed on a 1 km vertical grid; however, only every 5th contribution function is shown for clarity. The calculations were performed for conditions of a mid-latitude daytime atmosphere, SZA=60. See text for details.
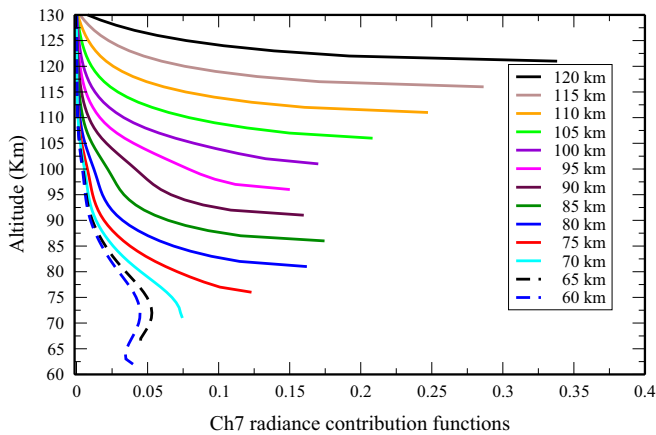
large optical thickness is immediately visible in this figure at tangent altitudes below ~70 km. Another optically thick region for SABER limb radiances in Ch7 is around 100 km (for the case of the climatological mid-latitude atmosphere). The tangent altitudes in the region above 70 km until 90 km have contribution functions fairly well peaked at the given tangent layers, so that most of the information comes from the tangent layer. This is a result of the physics of the population of the emitting levels as discussed. This is also true for tangent heights above ~115 km.

5. Retrieval algorithm

5.1. Introduction

One way to solve a non-linear inversion is to assume an a priori profile, which one supposes to be close to the true solution, and then iteratively solve the linearized version of the problem. All linear iterative methods seek a solution additively starting with

profile, $\mathbf{x_{init}}$, and through successive corrections obtain a solution of type $\mathbf{x_{sol}} = \mathbf{x_{init}} + \xi \mathbf{x_1} + \xi \mathbf{x_2} + \cdots$ (Twomey, 2002), where $\xi\mathbf{x}$ is the correcting term. If the linearization is appropriate, i.e., the "cost function" that is minimized is quadratic in the vicinity of the linearization point, then the problem retrain well defined statistical properties such that the error averaging kernels and covariance matrix can be calculated (Rodgers, 2000). If the linearization is not valid or the first guess not close to a solution then the problem may not converge at all, and, in addition, the problem does not retrain the Gaussian properties of error propagation (Tarantola and Valette, 1982; Rodgers, 2000; Twomey, 2002). The linear methods usually depend on explicit inversion of matrices which are in real application ill-conditioned (Twomey, 2002) and various regularization and/or a priori information must be applied to obtain a "physical" solution.

A more direct approach to non-linear inversion is using a re-laxation type algorithm where the initial guess is modified by multiplicative corrections, so that the final solution is of type $\mathbf{x_{sol}} = \mathbf{x_{init}} \times \xi \mathbf{x_1} \times \xi \mathbf{x_2} \times \cdots$ (Twomey, 2002). This type of algorithm has been shown to provide stable, reliable convergence and a very weak dependence of the solution on the initial profile (Chahine, 1972; Twomey et al., 1977). The disadvantage of these directly nonlinear methods is that there is no way to conveniently propagate statistical properties of the solution through the iterations. One of the solutions to this problem is to do a linear statistical analysis about the retrieved parameters through the relaxation inversion. Another approach is to perform an independent sensitivity analysis of the retrieval by varying different forward model parameters. The results of this approach can be sensitive to stopping criteria in the case of a small measurement S/N. Also, there is no obvious way to add an a priori information to the problem if available.

A very broad class of solutions designed to handle non-linear inverse problems is based on a random or quasi-random search of the entire parameter space, or "learning" the relationship between the data and state parameters from a training set. These methods are slowly finding applications for special problems (Tarantola, 1987; Sambridge and Mosegaard, 2002; Tamminen, 2004) however, are not suitable yet for larger scale inversions like needed for the SABER data mainly due to the prohibitive computational cost.

After several synthetic inversion studies, we have adopted an iterative relaxation algorithm retrieval approach, due to its low computational cost and stability. The retrieval method used in this study is an outgrowth of several previous methods developed and applied in the past, namely the onion-peeling (Russell III and Drayson, 1971), and a Chahine type relaxation algorithm modified with empirical corrections in order to achieve similar converge speed in both channels as discussed later. The entire inversion procedure starts with an initial guess for atmospheric parameters from which the non-LTE populations are calculated. Once the non-LTE CO_2 populations are known at all layers the limb radiances in Ch1 and Ch7 are calculated and compared against the measured radiances. If the difference is larger than a specified criteria, the initial atmospheric state is corrected based on a correction function. This process is repeated until the convergence criteria are reached. The quality of the overall fit is measured as root-mean-square $(1/\sqrt{Nalt}\,\|I_{mea}(z) - I_{cal}(z)\|)$, between measured and calculated radiances. The convergence criteria are set to NER/10 for each channel. A number of similar relaxation inversion algorithms were previously adopted for different inverse problems in remote sensing (Carlotti, 1988; Gusev, 2002; Mertens et al., 2003; Gusev et al., 2006).

5.2. Algorithm description and considerations

The simultaneous, self-consistent T_k/CO_2 retrieval is achieved through iteration over two independent retrieval modules of T_k and CO_2 VMR. During the T_k retrieval the values of CO_2 VMR are fixed, and during the CO_2 VMR retrieval the T_k is held constant. In this respect, the retrieval scheme used in this study and the scheme described in the paper by Mertens et al. (2003) are the same; however, the two schemes diverge from this point on in the detail considerations of the profile update functions, and in the general flow of the sequential updating of the two parameters. The first condition the retrieval algorithm checks is whether the $T_k(p)$ is close (converged) enough to the true profile based on the value of root-mean-squared (RMS) difference between the measured and calculated radiances. This initial step is taken because an incorrect temperature profile along with a hydrostatic equilibrium constraint on the pressure may dominate Ch7 radiance sensitivity above 80 km whereas even moderately incorrect CO_2 VMR (~10–15%) does not dominate the Ch1 sensitivity. In the subsequent
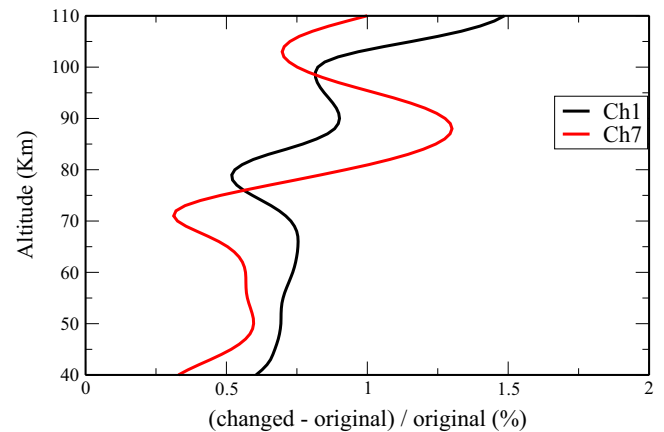

Fig. 10. Percent difference of limb radiance in Ch1 and Ch7 in response to global CO_2 VMR shifts by 2%. The calculations are performed for climatological mid-latitude conditions and SZA=60.

analysis we investigate the problem of coupling between 15 and 4.3 μm broad band channels, which leads to the difficulties with multi-channel inversion also encountered in previous missions. The nature of the retrieval problem is illustrated in Fig. 9. In the left panel (a) radiance response to a temperature increase without adjusting the pressure profile is shown, and panel (b) shows Ch1 and Ch7 response when the pressure is rebuilt hydrostatically after the temperature shift. In Fig. 10 the same radiance response is shown for a CO_2 VMR increase. Several features should be pointed out starting with panel (a) in Fig. 9. At 54 km, the limb radiance sensitivity to T_k in Ch7 matches those in Ch1, and is even higher than Ch1 sensitivity at lower tangent heights. This is a result of the Planck function at 4.3 μm being more temperature sensitive than at 15 μm; this is an important fact around the warmer region of the stratopause, where the LTE to non-LTE transition occurs. Second, there is an inverse temperature response of Ch7 radiance at 72 km (Fig. 9), despite the fact that 4.3 μm emissions at these tangent heights are already significantly influenced by non-LTE. A smaller contribution to this effect comes from the temperature dependence of the V–T and V–V processes influencing the 4.3 μm transitions. First, there is an inverse temperature dependence of the V–V CO_2–N_2 rate, and then there is the V–T process of splitting ν_3 quanta into ν_2, which has a rate proportional to the temperature.
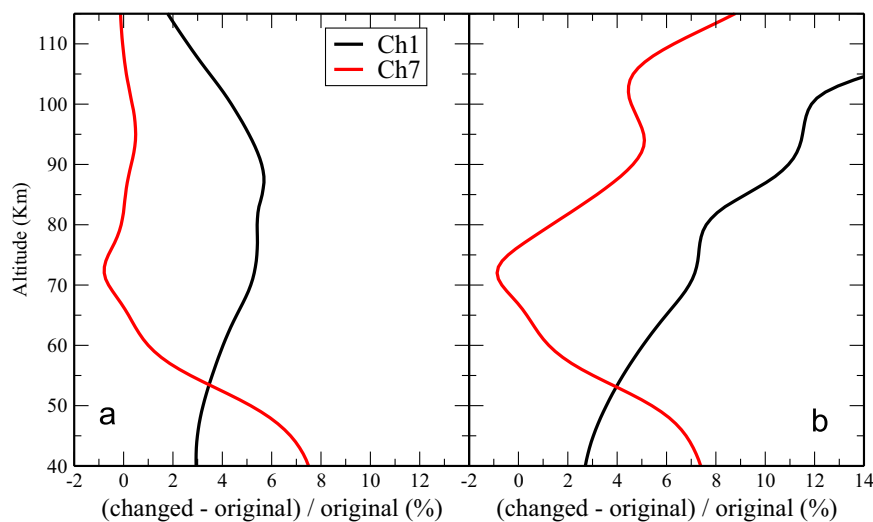

Fig. 9. Ch1 and Ch7 sensitivity to global temperature shifts. A percent difference of limb radiances for Ch1 (black) and Ch7 (red) curve to a global shift of temperature by +2 K. The calculations are performed for climatological mid-latitude conditions and SZA=60. The pressure was not hydrostatically adjusted as T_k changed in the case shown in panel (a). The panel (b) shows the same, but this time the pressure was recalculated using the hydrostatic equation. (For interpretation of the references to color in this figure caption, the reader is referred to the web version of this paper.)

However, the explanation rests with the fact that changes in T_k result in redistribution of opacity among bands, and not because of temperature dependence of rates, as detailed below. The main contribution to the Ch7 limb radiance in this region comes from the SH bands. As the T_k increases the population of upper levels of the 15 μm FH transition (which are in LTE at this altitude) are also enhanced, which results in even larger self-absorption of 4.3 μm radiation in the SH bands since the upper levels of the 15 μm FH transition are the lower level of the 4.3 μm SH transition (see level diagram 2). Hence, even less radiation escapes from the atmosphere at these tangent heights as T_k increases. On the other hand, the weaker inverse dependence of Ch7 limb radiance on T_k at around 110 km is related to the inverse dependence of the collisional V–V rate ($K^{V-V}_{O(^1D)-N_2}$ and $K^{V-V}_{CO_2-N_2}$) on T_k, which results in a smaller pumping rate of the 4.3 μm FB as T_k increases.

An important lesson is learned from Fig. 10. Above tangent heights of about 100 km and below ~75 km the Ch1 limb radiances exhibit a well behaved sensitivity to CO_2 VMR changes that is stronger than the Ch7 radiance response to the same changes. However, above about 60 km the Ch1 limb sensitivity to CO_2 VMR change is about a factor of 5 smaller than the T_k shift for the given perturbations. In the case of Ch7 limb radiance response to the CO_2 VMR shift, it is of the same order at 55–60 km and significantly less below 55 km than the response of the same channel to the T_k shift. This further explains why it is not possible to proceed with the standard two channel retrieval much below 60 km without increasing instability of the retrieval. In addition, the sensitivity curves intersect at different altitudes and may exhibit similar slopes over some limited altitude ranges, meaning that there are not always two independent pieces of information available to determine the two unknown profiles.

Finally, the coupling of these two channels is revealed in the (panel b) of Fig. 9. The hydrostatic constraint on the pressure contributes to the non-linearity of the two-channel retrieval as the pressure and density at a given tangent height depends on T_k at all altitudes below.

Nevertheless, during the retrieval iterations, the preliminary check on the $T_k(p)$ ensures that this parameter is "relaxed" enough (which usually happens within 1–2 iterations of the $T_k(p)$ retrieval module), to eliminate large corrections in the CO_2 retrieval module due to an incorrect density profile. This condition is static and relevant only for the very first couple of iterations, because once passed it is never rechecked again.

Once this first condition is met the two-channel self-consistent retrieval iteration begins with iteratively switching between the two relaxation modules of T_k and CO_2. One global iteration is defined as performing one pass through the T_k module with a subsequent pass through the CO_2 retrieval module. The next check is whether the CO_2 VMR profile is converged. Again, this is determined based on the RMS differences between the measured and calculated radiances for Ch7. If the RMS difference is larger than a user prescribed value, the CO_2 VMR profile is updated. A typical converged profiles fit the measured radiance to within 0–1% in both channels in the case of self-consistent studies (i.e. only T_k and CO_2 VMR are unknown). Application of the inversion algorithm to the actual SABER measurements gives retrieved profiles radiances that agree to within 0–5% with the measured radiances in both channels; Ch7 usually shows better agreement (2–4%). The larger differences between measured and synthetic radiances occur due to several factors: (1) in self-consistency studies the atmospheres below and above the inversion grid are assumed known, (2) the uncertainties in the auxiliary inputs may enter the inversion collectively in a strongly non-linear way (either amplifying or damping) the random noise features, (3) channel coupling may be larger due to (1) and/or (2), and (4) the random noise may

be larger than the 1-sigma NER assumed in the synthetic calculation. Nevertheless, in all the inversion cases the RMS difference between the measured and calculated radiances is significantly reduced for the final retrieved profiles compare to the starting ones.

It is well known that a high degree of fitting between calculated and measured radiances (i.e. convergence in the measurement space) is not a sufficient condition to have a convergence in the parameter space. It is possible to diverge from a solution in the parameters space, while fitting radiance to within a fraction of percent (well known problem of ill-conditioning as well as non-linearity of the inverse problem). For this reason, illustrating converged profiles in the parameter space is less ambiguous, therefore, we present converged solutions in the parameter space in subsequent figures and discussions.

Upon exiting the CO_2 retrieval module, a flag is set so the algorithm "knows" that the next step is to perform a T_k retrieval, rather than to continue fitting the CO_2 VMR. Because the relative CO_2 non-LTE populations depend weakly on the CO_2 VMR, and only a single correction to the CO_2 VMR profile is made at a time, the non-LTE populations do not have to be recalculated after exiting the CO_2 retrieval module. This fact was also exploited by Kaufmann et al. (2002). With the updated CO_2 VMR profile, only the limb radiances are recalculated. Then the algorithm proceeds into the T_k retrieval module. If the $T_k(p)$ is not converged, an update of the temperature profile is obtained in the T_k retrieval module. There, a flag is set to indicate that the next iteration should go to the CO_2 module. The pressure is rebuilt after the new T_k is obtained using the hydrostatic equilibrium relation. Then, with the new T_k and pressure profiles the non-LTE problem is solved to obtain new vibrational level populations with which the next global iteration can proceed.

It was found that to achieve stable convergence the temperature and CO_2 relaxation must be convergent at a similar speed; otherwise there is considerable error propagation (systematic and/or random) from the slower into the faster converging modules. The final form of the temperature correction function is given by $T_i^{n+1} = T_i^n \times [\sum_j (I_j^m/I_j^c) G_{ij}]^A$, which uses a modified Chahine update function. Here, i and j iterate the tangent heights and n is the iteration counter. I_j^m, I_j^c is the measured and calculated radiance for height j, and after several numerical experiments the elements of G_{ij} were set to zero everywhere except at tangent height $i+1$, since the radiance sensitivity is shifted to a grid point below the current tangent height (Rezac et al., 2011). The critical parameter for the convergence is the exponent A in the above formula, which was found through numerical experiments to be 0.23 for a fast but still stable convergence. In the CO_2 modules, the update function is given by $x_i^{n+1} = x_i^n \times [(I_i^m/I_i^c)]^B$, where x_j is the CO_2 VMR at height j. The exponent B is applied to adjust the convergence speed, and was found to be 0.8. In the case of the CO_2 update function there is no need to utilize the weighting filter matrix, G_{ij} as was done for the T_k update function since changes in the CO_2 VMR affect the optical depth along the LOS rather than the volume emission, i.e. the source functions (see details in Rezac et al., 2011). In both modules, the entire profiles are updated at once for each iteration. This greatly speeds up the inversion and avoids profile oscillations that, for example, the "onion-peeling" technique was prone to develop in our tests.

5.3. Algorithm: self-consistency

It was found during self-consistent studies that if the only unknowns in the inversion problem are the $T_k(p)$ and the CO_2 VMR, the simultaneous, self-consistent retrieval approach has no problem stably converging to the true profiles. Numerous starting

conditions tested for different T_k/CO_2 profile shapes indicate that the solution is found within 14 global iterations in the worst case. If the assumed forward model parameters (those that are not retrieved, such O, O(^{1}D), and/or collisional rate coefficients) possess strong biases, the retrieval algorithm will transfer them on to the solution thereby producing biases on the CO_2 VMR and temperature, in which case the convergence could be significantly slower and/or it may become unstable. From this stand point it is undesirable to fit differences between measured and calculated radiances originating from errors in other parameters by adjusting the T_k and CO_2 VMR. Therefore, when the two-channel retrieval is applied to the real measured SABER radiances, only 14 global iterations are allowed.

The random noise in Ch7 is negligible over the entire retrieval altitude range and does not influence the relaxation (as shown later). However, the radiance noise in Ch1 becomes noticeable above a tangent height of about 80 km. It is best to avoid fitting the noise features because it leads to oscillation in other atmospheric parameters and may negatively affect the non-LTE calculation as T_k profile influences the collisional V–T, and V–V rates. Therefore, a vertical smoothing of the T_k profile is applied with a moderate 2 km wide moving average over the retrieval altitude range every 4 global iterations. Since, it takes on average 6–12 global iterations to relax both parameters, this smoothing is usually applied no more than three times. In the language of inverse theory, the smoothing of the T_k profile can be regarded as regularization, since a constraint is imposed on the nature of the solution (i.e. smoothness) that does not come from the measurement. The smoothing limits how well the measured signal can be matched but also provides a smaller variance of the retrieved parameters. During iterations the Ch1 random noise may propagate into the CO_2 retrieval especially at the high altitude boundary for Ch1. Therefore, smoothing with a 2 km wide moving average is also applied to the CO_2 VMR profile every 4 global iterations. Because the CO_2 VMR profile is generally monotonic over broad altitude ranges, the mild smoothing degradation has little impact on the CO_2 VMR profile information.

As any strongly non-linear inverse problem, the two-channel retrieval shows some dependence on the initial conditions with more so on the $T_k(p)$ parameter. The self-consistent synthetic retrievals showed that the maximum deviation of the initial profiles of T_k and CO_2 from the true one, for which the algorithm still remains stable and converges to the solution, is in the range ± 15 K and $\pm 20\%$ for CO_2 VMR applied as global shifts. The initial atmospheric profiles in actual application to the SABER data are expected to be well within these limits, especially at the lower retrieval boundary as we rely on SABER operational temperatures as an initial guess. To illustrate the self-consistency of the described algorithm we performed several case studies starting from different initial conditions for temperature and CO_2. An example shown in Fig. 11 demonstrates the algorithm performance in the perturbed condition with a sine wave form of 10 K amplitude and 10 km vertical wavelength. The starting CO_2 VMR profile exhibits large deviations from the original in the upper mesosphere (>20%).

The left upper panel (a) shows the original, initial and retrieved temperature profiles, and the upper right panel (b) has the same for the CO_2 VMR profile. The two lower panels (c) and (d) show the retrieval error as a function of altitude in case of temperature and CO_2 VMR respectively (i.e. the parameter space). The relaxation algorithm recovered the original profiles for both parameters with very good clarity. The T_k profile converged to within 1–2 K with larger values (3–5 K) near the boundaries and the CO_2 converged to within 2% everywhere except at 102 km, which has a negative deviation of 6%. The interdependence of the channels is manifested in the CO_2 error pattern which shows a weak wave structure coming from the T_k retrieval. However, there is no indication of instability of the relaxation algorithm that would translate into unwieldy artificial structures either in the retrieved T_k or the CO_2 VMR profile. The radiance fitting is in the range of 0.5% in Ch1 and in the range 0–0.5% in the Ch7 and the convergence was reached within 12 iterations, which is usually the case for the great majority of the tested profiles obtained during self-consistency studies. Another test case of particular interest for further discussion is shown in Fig. 12. The temperature profile has very small scale
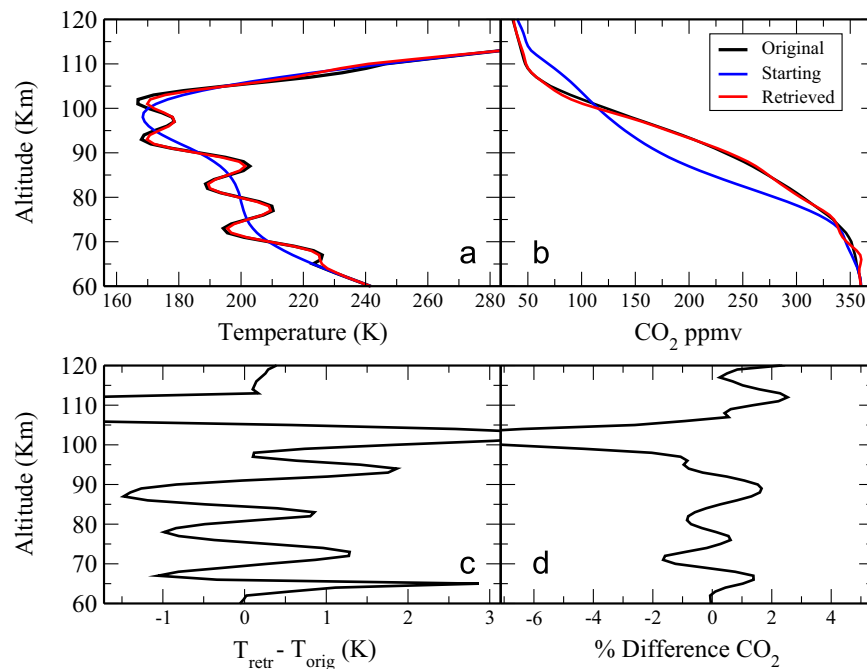

Fig. 11. Case 3: self-consistency test of the two-channel retrieval algorithm for a climatological tropical atmosphere with a sine wave perturbation. Black curve is the original profiles to be retrieved, blue curve shows the initial profiles, and the retrieved profile is shown in red. See text for discussion. (For interpretation of the references to color in this figure caption, the reader is referred to the web version of this paper.)
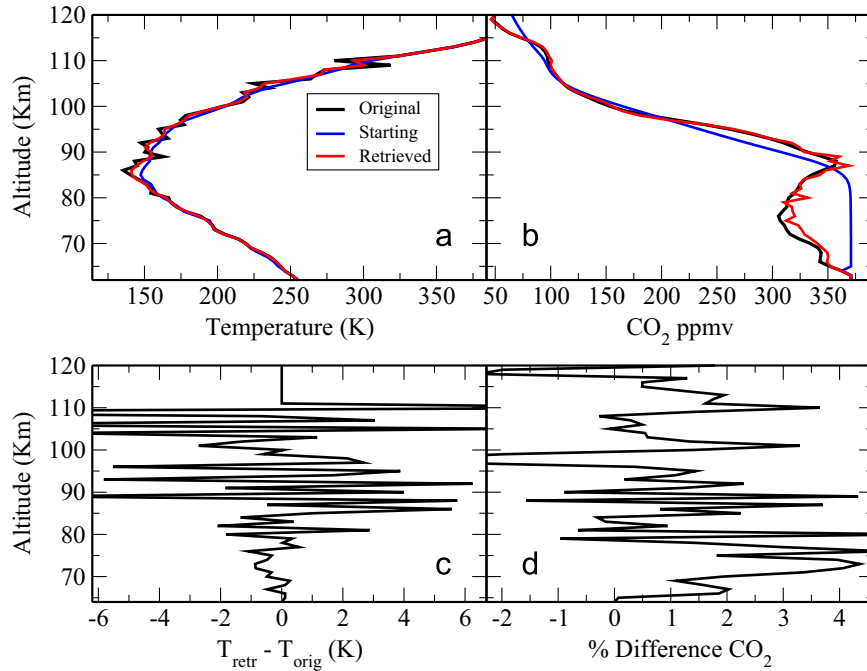
Fig. 12. Case 4: self-consistency test of the two-channel retrieval algorithm with fine scale T_k structure and complex CO_2 structure. The curves are color coded similar to Fig. 11. See text for further explanation. (For interpretation of the references to color in this figure caption, the reader is referred to the web version of this paper.)

vertical oscillation and waves. The starting T_k profile is within 3–15 K of the true profile but is smooth. The starting CO_2 VMR profile is taken from the mid-latitude climatology. Again, the panels (a) and (b) show the original, initial, and retrieved profiles in case of temperature and CO_2 VMR. In the lower left panel (c), the T_k retrieval error is plotted and panel (d) shows the same for the CO_2 VMR. The temperature errors are in the range of 2–4 K with somewhat larger values of 6–8 K appearing as spikes at altitudes where the fine scale temperature structure is not well retrieved.

The complex original CO_2 vertical structure is retrieved over the entire altitude range with retrieval errors within 2–4%. The relaxation algorithm was able to converge to the original CO_2 VMR profile even in the optically thick region at 70 km without exhibiting instabilities. However, due to the coupling of the two channels some of the small scale temperature structure was transferred to the CO_2 profile, which is also clearly visible.

The case study shown in Fig. 13 is for a typical polar summer temperature profile. In this case we have one initial profile for T_k,
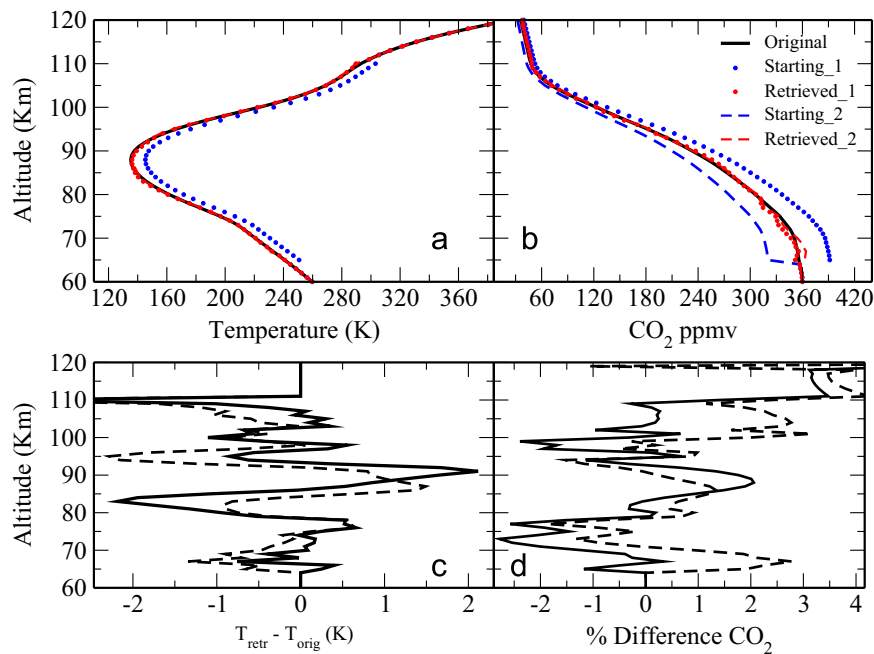

Fig. 13. Case 5: self-consistency test of the two-channel retrieval algorithm for polar summer temperature profile and two different initial conditions on the CO_2 VMR. See text for further explanation of initial conditions and color coding, which is similar to the previous figures, except here we have two retrieval error profiles in the panels (c) and (d), corresponding to the two different initial conditions in CO_2 for a given starting temperature profile. The full black line corresponds to the initial conditions shown as blue dots in panels (a) and (b), while the dashed black line corresponds to the dashed blue line initial conditions in panel (b) and dot in panel (a). (For interpretation of the references to color in this figure caption, the reader is referred to the web version of this paper.)

shown in blue dots in panel (a), and two initial profiles for CO_2 VMR (higher and lower than the true profile) shown in panel (b). In this case the initial profiles are scaled as -10 K for temperature and $\pm 10\%$ for the CO_2 VMR. In the panels (c) and (d) the retrieval error profiles for temperature and CO_2 VMRs are shown. The two black (full and dashed) lines in panels (c) and (d) correspond to the two CO_2 initial profiles, higher/lower respectively. The important features to note are that the inversion is stable in the measurement space (figure not show) and, most importantly, in the parameter space. The retrieved profiles are within 2 K and 2% of the true profiles, with higher values near the upper/lower boundary of the retrieval grid, which is a well understood feature. We also point out that there are no large scale peaks and/or artifacts in the CO_2 VMR or the temperature profiles, which would compromise the physical interpretation of the profiles. Finally, a small dependence on the initial conditions is observed as slightly different error patterns for the two black curved in panels (c) and (d). Similar numerical experiment was done for T_k lower than the true profile and for the same (two) CO_2 initial profiles, which yield a similar result (figure not shown).

In summary, for the self-consistency, the ill-posed nature of the two-channel inversion results in non-zero retrieval errors and sometimes leads to error transfer between the channels. Nevertheless, an important result is that the retrieval algorithm does not introduce severe biases or artificial vertical structures in the retrieved parameters for any of the different initial atmospheric conditions tested during these studies.

5.4. Sensitivity and error analysis

In this section the most important sources of uncertainties and their effects on the inferred T_k/CO_2 are discussed. The total uncertainty of the retrieved quantities is separated into two components: (1) the random error which gives a measure of achievable precision, and (2) the systematic error which provides information on the bias of the inferred quantities. In practice, however, it is not always clear how to correctly identify these two components. For instance, in the atmospheric regions with strong temporal or spatial variability, single profile biases resulting from certain atmospheric parameters may vanish when averaged over certain time and/or space domain. In this case certain biases might be regarded as a quasi-random component on average. The purely random component affecting the retrievals is the random noise of the radiometer system. The important sources of the systematic component are instrument calibration, non-LTE modeling parameters such as rate coefficients, and possible biases in other assumed atmospheric abundances.

An important aspect of the simultaneous retrieval algorithm is that the error analysis has to be performed in both channels at the same time, because of the interdependency of the broadband channels on both T_k and CO_2 as described in Section 5.2. This means that, for example, non-LTE processes influencing predominantly populations of the ν_3 emission from which we obtain the CO_2 VMR can be indirectly reflected in the temperature profile inversion which relies on the ν_2 emissions. Since the inverse problem is non-linear, estimating uncertainties in each channel independently, as done in single channel inversions (Kaufmann et al., 2002; Gusev et al., 2006; García-Comas et al., 2008), is not entirely appropriate in the case of simultaneous inversion.

The mean retrieval errors due to the various sources for a single profile of T_k and CO_2 are displayed in Tables 1 and 2 respectively along with the combined total error. The single profile error is calculated as an average over four different atmospheric input conditions: equatorial equinox, low- mid-, and high-latitude condition of the summer hemisphere.

The uncertainty due to the random noise in the radiometer

Table 1
Two-channel kinetic temperature retrieval errors and their sources for a single profile.

Errors source[a]	Altitude (km)				
	70	80	90	100	110
Random noise[b]	<1	±1	±3	±4	±6
Radiance bias	<1	<1	<1	<1	<1
$P(z=0)$ bias[c]	±2	<1	±1	±2	±2
$T(z)$ bias	±2	±1	±1	±2	±5
Atomic O bias	±1	±1	±2	±7	±19
$O(^1D)$ bias	±2	±1	±1	±3	±6
k_{VV} N_2–$O(^1D)$	±1	±1	±1	±3	±3
k_{VT} CO_2–O	±1	±1	<1	±8	±20
k_{VT} $CO_2(\nu_3-\nu_2)$[d]	±3	±1	±1	±1	±1
k_{VV} CO_2–N_2	±5	±3	±2	±3	±5
Root-Sum-Squared	±8	±5	±5	±13	±30

[a] Temperature uncertainty are in units of (K).
[b] SABER NER values for each channel respectively.
[c] Reference pressure at 30 km.
[d] Splitting of ν_3 quanta into 1–4 ν_2 quanta in V–T collisions with N_2.

Table 2
Two-channel CO_2 VMR retrieval errors and their sources for a single profile.

Errors source[a]	Altitude (km)					
	70	80	90	100	110	125[b]
Random noise[c]	<1	<1	±1	±1	±2	±2
Radiance bias	±3	±2	±1	±2	±1	±2
$P(z=0)$ bias[d]	<1	±2	±4	±4	±3	±4
$T(z)$ bias	±1	±4	±6	±6	±4	±4
Atomic O bias	±1	±1	±2	±7	±13	±10
$O(^1D)$ bias	±12	±5	±5	±14	±23	±13
k_{VV} N_2–$O(^1D)$	±5	±3	±3	±9	±11	±8
k_{VT} CO_2–O	±1	±1	±1	±2	±5	±5
k_{VT} $CO_2(\nu_3-\nu_2)$[e]	±14	±3	±3	±3	±4	±3
k_{VV} CO_2–N_2	±28	±17	±6	±3	±10	±6
Root-Sum-Squared	±35	±19	±12	±21	±32	±22

[a] CO_2 uncertainty are in (%).
[b] CO_2 VMR retrieved at altitudes between 115 and 130 km relies on the WACCM input. While these are consistent with each other, the parameters such as O and $O(^1D)$ are not known very accurately. For these reasons the error may be in reality larger than indicated (assumed accuracy of 50%).
[c] SABER NER values for each channel respectively.
[d] Reference pressure at 30 km.
[e] Splitting of ν_3 quanta into 1–4 ν_2 quanta in V–T collisions with N_2.

system is estimated separately for each channel by adding normally distributed noise to the synthetic radiances with a standard deviation equal to the noise equivalent radiance NER for each channel. The NER in the Ch7 is very small $[7.35 \times 10^{-11}$ W/(cm^2 sr)] providing very high signal-to-noise ratio and, therefore, it does not influence the daytime two-channel retrieval significantly. The Ch1 NER $[2.45 \times 10^{-8}$ W/(cm^2 sr)] (Russell III et al., 1999) does impact the T_k retrieval especially above 90 km. It also indirectly influences the CO_2 VMR retrieval as discussed previously, which is reflected in Table 2.

The absolute calibration of the SABER instrument has shown remarkable stability over the 13 plus years of the mission. The total scale factor changes over the life of the mission to this point are <0.2% and <2% for the CO_2 15 µm and 4.3 µm channels respectively. The actual scale factors are continuously monitored in-

flight as part of a routine calibration procedure, and are accounted for in the data processing. So while these factors are a measure of instrument stability, they do not indicate a radiance error; rather they can be viewed as upper limits on possible error. The scale factor is also dependent on the Focal Plane Array (FPA) temperature which is continuously monitored and accounted for in the calibration procedure. The in-orbit scale factor determination is used as a transfer standard to tie the in-orbit measurement to the absolute ground calibration which is known to on the order of 0.5% or better. Instrument FOV far field wings (off-axis effects) and side lobe effects were measured in the ground calibration to within a few percent using standard "knife edge" and "hot wire" calibration techniques respectively. These properties are included in the radiometric modeling of the signals used in the retrieval process and they have been verified in flight using lunar scans. This detailed attention paid to calibration gives good confidence in the instrument radiometric accuracy. The uncertainties under the "radiance bias" entry in Tables 1 and 2 were calculated for radiance bias of a 1% in the Ch1 and 1.5% in the Ch7, which is slightly larger than the expected absolute calibration uncertainties.

Next, a reference pressure error is considered. The $p_0=p$ (30 km) is varied within the estimated maximum range of $\pm 4\%$ derived as $\sim 2\sigma$ from deviations of geopotential height between SABER and Met Office analysis presented in Remsberg et al. (2003). Changing p_0 would alter the temperature retrieval in the LTE region (i.e., below the lower boundary of the two-channel retrieval) but it is kept unchanged in determining this uncertainty. Therefore, this error reflects only the influence of the p_0 at the altitudes relevant to the two-channel retrieval. The combined effect of the $T_k(p)$ bias is considered separately in the next row in the table, labeled T_k bias. This bias was estimated by shifting the temperature profile at all altitudes (even below and above the retrieval grid boundaries) by ± 5 K and adjusting the pressure through the hydrostatic equation. This particular T_k range was used based on findings presented by Remsberg et al. (2008) regarding the stratospheric and lower mesospheric biases in the v1.07 temperature product in comparison with correlative measurements from other instruments. The goal is to estimate what effect the bias in the stratospheric T_k profile has on the two-channel retrieval in the MLT region. The errors due to the stratospheric bias in $T_k(p)$ are affecting the retrieved T_k profiles noticeably less than it is influencing the retrieved CO_2 VMR. This is mainly due to the introduced pressure bias with the errors slowly growing with altitude.

Estimating the atomic O and O(^{1}D) errors is difficult due to their natural variability in space and time. The v2.0 SABER data provide retrieved O and O(^{1}D) VMR profiles up to altitudes of about 90 km where it is smoothly joined into WACCM model values. Unfortunately, the effect of atomic oxygen becomes most important above 90 km predominantly influencing the T_k retrieval. The retrieved CO_2 VMR is not directly sensitive to atomic oxygen uncertainties (only for a large perturbation O VMR the removal of N_2(1) is increased noticeably). However, during 2-channel inversion the growing T_k error (which is sensitive to atomic O) is reflected in the CO_2 VMR errors. The uncertainties in the O(^{1}D) VMR profile can be reflected strongly in the retrieved CO_2 VMR, especially in the altitude regions around 70 and 110 km, i.e., where the opacity is large and the 4.3 μm FB dominates the total radiance. At 110 km, the CO_2 VMR error reaches 23% but decreases above as the opacity gets smaller. The upper and lower limits on the O and O(^{1}D) VMR uncertainty are taken to be $\pm 50\%$. On average the assumed range of uncertainty of these two parameters could be an overestimation. However, due to very strong temporal and spatial variability of these parameters in the upper MLT, right around the region where they come mostly from the model values, this uncertainty range may be realistic on a profile to profile basis. More

detailed discussion on the SABER atomic O uncertainty, which is estimated between 10% and 30%, can be found in Mlynczak et al. (2013) along with discussion on comparisons with other datasets. More recently Kaufmann et al. (2014) found the SABER atomic O to be about 30% higher than abundance derived from SCIAMACHY instrument.

In the subsequent discussion on the retrieval uncertainties, it should be kept in mind that we are dealing with 2-channel non-linear inversion, meaning uncertainties have to be studied as a "bulk" response on both retrieved profiles given a perturbation of a atmospheric parameter (atomic O or O(^{1}D) in this case). The non-LTE processes can be separated only to a degree without a detriment to the estimated errors. For example, imposing a bias on atomic O, the following chain of effects in its entirety is taken into account during the 2-channel inversion: (1) atomic O modifies the amount of $CO_2(\nu_2)$ reservoir, which in turn modifies ro-vibrational partition function (through changes in T_{vib}), and influences the 4.3 μm bands. The ν_3 levels are affected indirectly since the N_2(1) reservoir changed as a result of the V–T process with atomic O. Then, during the inversion iterations we modify the T_k in order to fit radiance in Ch1, which results in changes to the V–V processes (inverse T_k dependence) influencing the ν_3 quanta. Subsequently, when we change CO_2 VMR we modify opacity and to some degree a source function depending on altitude. Therefore, the estimated uncertainties in Tables 1 and 2 reflect all these effects naturally, including the feedback of CO_2 VMR from biases in T_k and vice versa.

It should be pointed out that the atmospheric or non-LTE parameters strongly impacting the $CO_2(\nu_3)$ populations, the ones associated with atomic oxygen and O(^{1}D) energy transfer, yield a non-symmetric error profile in the retrieved CO_2 VMR as illustrated in Fig. 14. Furthermore, the amplitude of the asymmetry varies with altitude. For example, CO_2 VMR profile errors around 110 km caused by the O(^{1}D) VMR bias of $+50\%$ are smaller by about 60% compared to CO_2 VMR retrieval error when the O(^{1}D) is decreased by the same amount. Despite the asymmetry in the error profiles we provide an average of the deviations in Tables 1 and 2. As previously pointed out, these biases are likely distributed in quasi-random manner in latitude and season.

Next we discuss retrieval errors related to uncertainties in the non-LTE quenching rates of the $CO_2(\nu_2, \nu_3)$ levels. The electronic-vibrational energy transfer between the excited O(^{1}D) and N_2,
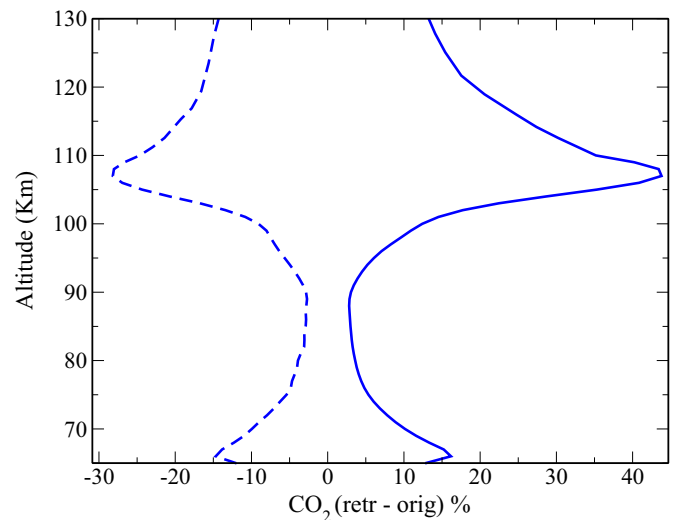

Fig. 14. Altitude profile of the CO_2 retrieval error (%) with respect to global shift of O(^{1}D) VMR for equinox equator temperature profile. The dashed line corresponds to an increase of O(^{1}D) VMR by 50% and the full line shows the response of a decrease by the same amount.

labeled in the table as $k_{VV}(N_2-O(^1D))$, has three sources of in-accuracies: (1) the branching ratio of the reaction for the various vibrational states of N_2, (2) efficiency of cascading down from $N_2(v > 20)$ to $N_2(v = 1)$, and (3) the accuracy of the V–V rate itself. In addition, this rate is inversely dependent on temperature. In this study we assume an uncertainty for this rate of $\pm 30\%$ which affects mostly the CO_2 VMR retrieval at 70 and 110 km, with an error pattern nearly identical to that shown in Fig. 14.

The V–T collisional rate coefficient for the process $CO_2(\nu_2)$–O plays an important role in determining the populations of $CO_2(\nu_2)$ levels and, therefore, the retrieved T_k. However, a large discrepancy (more than factor of 4) exists between the laboratory measured value, the value needed in dynamical models, and the value needed to infer T_k from satellite measured emissions. Despite this fact, the value of this coefficient is well established to be 6×10^{-12} in order to obtain physical temperature profiles from the measured radiances (Kaufmann et al., 2002; Gusev et al., 2006; Remsberg et al., 2008; García-Comas et al., 2008; Feofilov et al., 2012). The papers by García-Comas et al. (2008) and Feofilov et al. (2012) discuss in detail the literature review for different values reported for this rate coefficient. The range of values of this rate used in context of non-LTE radiance modeling lead us to accept a $\pm 50\%$ uncertainty on this parameter. The effects on the retrieved T_k coming from this process are very similar in magnitude and altitude error profile to the atomic oxygen bias, since the collisional $CO_2(\nu_2)$ rate is a product of the two quantities. This is not true for the error propagation into CO_2 VMR, which is not directly very sensitive to this rate coefficient as it impacts predominantly only the ν_2 levels. The atomic O variations does directly influence both, the ν_2 and ν_3 levels (through N_2–O collisions as discussed above). However, the CO_2 VMR error still reflects the T_k biases as far as they propagate through pressure changes and V–V

dependence.

Another important source of error in the inferred CO_2 VMR, mostly below 80 km, comes from the uncertainty in the V–T quenching rate in the reaction $CO_2(\nu_3) + N_2$ and O_2 that leads to the splitting of ν_3 quanta into 1–4 $CO_2(\nu_2)$ quanta. The branching ratio is temperature dependent and was taken from the work of Shved et al. (1998). The inaccuracy of this rate is considered to be $\pm 50\%$ (Kaufmann et al., 2002) and it results in a relatively strong bias of 14% in the CO_2 VMR retrieval at 70 km; but above 80 km, this error remains almost constant with altitude. The bias in the CO_2 VMR is directly responsible for the temperature bias of 3 K around the 70 km altitude range.

The uncertainty in the V–V rate between $CO_2(\nu_3)$–$N_2(1)$ is of crucial importance to the modeling of Ch7 limb radiance. Even though this rate coefficient has been measured in the laboratory, an analysis of the SAMS satellite experiment 4.3 μm radiances suggest a rate that is larger by a factor of 2 (López-Puertas and Taylor, 1989). Therefore, the uncertainty for this rate is assumed to be $\pm 50\%$ and it constitutes the largest contribution to the total error in the retrieved CO_2 VMR below 80 km. Near the mesopause the VMR error is minimum, but increases again near 110 km to 10%. This rate is also inversely dependent on the temperature, which means as the CO_2 VMR increases/decreases during the retrieval iterations, the temperature will decrease/increase, hence slightly offsetting the effects into the CO_2 VMR uncertainty. The temperature retrieval is affected mostly indirectly through biases in the CO_2 VMR. A summary of error patterns in the retrieved CO_2 VMR from the above discussed source is presented in Fig. 15.

We assume no additional errors, such as isotopic fractionation, its altitude dependence (constant), and spectroscopic parameters such as, broadening parameters and their temperature dependence, Einstein spontaneous emission coefficient. We tested the
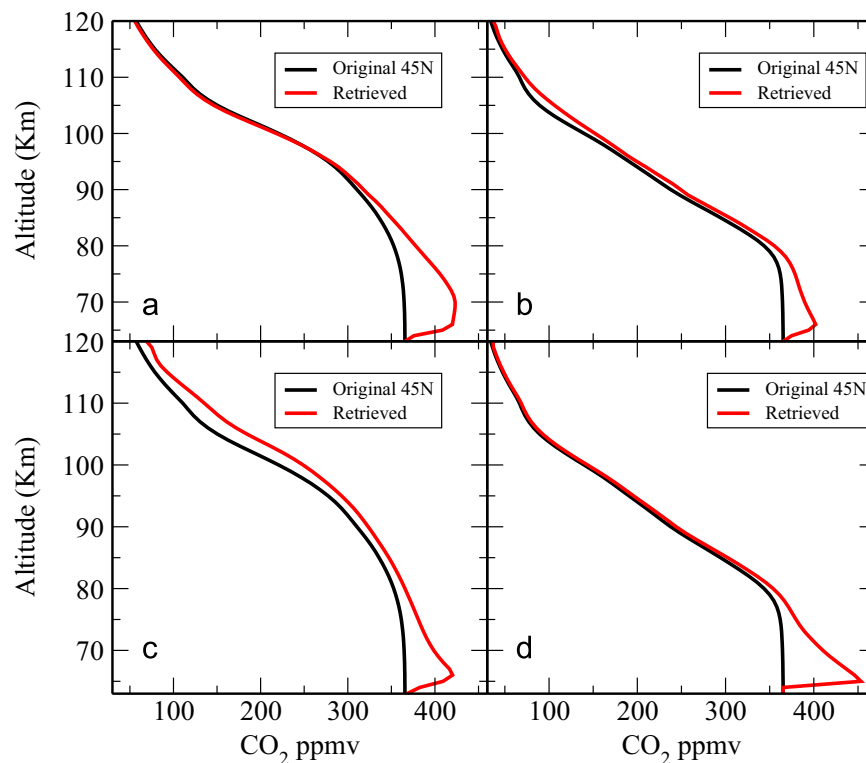

Fig. 15. Assessment of the general altitude error profiles in the retrieved CO_2 VMR for the four most important cases. Panel (a) shows the original CO_2 VMR (black curve) and retrieved CO_2 VMR profile (red curve) for the case of an enhanced V–V coefficient by $+30\%$ between $CO_2(\nu_3)$ and N_2. The panel (b) shows the same two curves for the case of decreasing the V–V rate by 30% between $O(^1D)$ and N_2. The bottom left panel (c) corresponds to the case of decreasing $O(^1D)$ VMR by 50% and the bottom right panel (d) shows the effects of increasing the rate of V–T process that leads to splitting of the ν_3-quanta into ν_2-quanta by 50%. In all four selected cases there is a significant bias developed in the retrieved CO_2 VMR around 65–75 km, as already noted before, however, none of them can be responsible for the polar summer case anomalous profile as described. (For interpretation of the references to color in this figure caption, the reader is referred to the web version of this paper.)

sensitivity to Einstein A coefficient which are typically known with high accuracy for the fundamental bands and increasing up to ~3% for hot bands (Rothman et al., 2009). We tested higher end (3%) of this uncertainty on the Einstein coefficient of FH, SH bands, and found less than 1% radiance deviation in both channels, however, Ch7 increases (2.0%) above 115 km for the tested case. The radiative transfer module used in this work is the same as applied by Feofilov et al. (2009), which has been validated against the radiative transfer code of GATS Inc. (Marshall et al., 1994) and the KOPRA codes (Stiller, 2002) with differences less than 1%. In comparison, the effects of these uncertainties are very small relative to the previously described uncertainties in non-LTE quenching rates, atomic O and/or $O(^1D)$ VMR.

5.5. Algorithm application to the SABER v2.0 measurements

Once the self-consistency of the algorithm was established the algorithm was applied to the real SABER measurements for several hundred test cases under various atmospheric conditions. An unexpected but persistent pattern was observed in the retrieved CO_2 VMR predominantly near polar summer latitudes. It should be noted that the retrieval algorithm still remains stable and the convergence in terms of RMS between the measured and calculated radiances proceeds normally as for any other case. To illustrate this we show in Fig. 16 several profiles of Ch7 radiance ratios (measured/calculated) at the first iteration of the CO_2 retrieval, i.e., radiances are calculated with WACCM CO_2 as an initial profile for polar summer latitudes. It is obvious from these ratios that in order to fit the measured radiances, such that the ratio ≈ 1 around 90 km, we have to increase the CO_2 VMR.

As pointed out earlier, fitting the Ch7 radiances (in polar summer latitudes) results in a sharp peak developing in the CO_2 VMR profile centered between 87 and 93 km. There is also usually a broader minimum in CO_2 VMR, "knee", at around 77 km, however, it can sometimes be a secondary maximum. The pattern in space and time of this 77 km "knee" shows some variability. We show example of a retrieved profile with the 90 km feature developed in Fig. 17.

The minimum in this profile could not be explained by limb geometry alone, when viewing through the 90 km peak. For profiles measured more toward the summer hemisphere mid-latitudes, this feature fades out. Additionally, these profile features do not develop at high latitudes of either hemisphere during equinoxes. Once this feature was shown to be persistent, extensive tests have been carried out on the inversion algorithm itself to
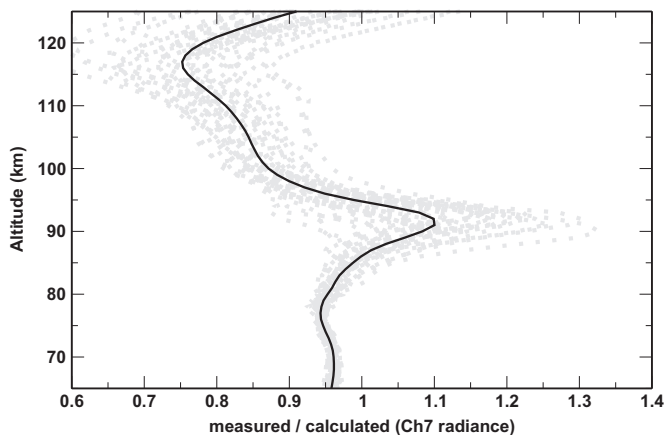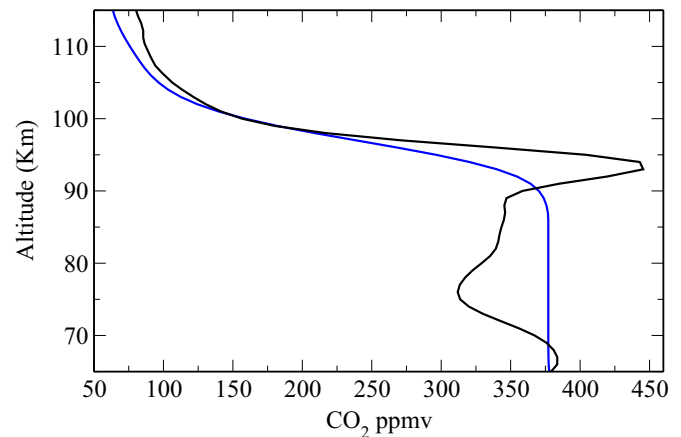

Fig. 17. An example of the 90 km "feature" developing in the retrieved CO_2 VMR in the summer hemisphere at high latitudes. This example is for a day-of-the-year 196, 2003 at latitude 77° north. The black line is the unconstrained CO_2 VMR retrieval and the blue line shows the initial profile from the WACCM model. (For interpretation of the references to color in this figure caption, the reader is referred to the web version of this paper.)

make sure that it is not caused by the inversion process itself. We have checked rigorously using numerical experiments that the inversion for polar summer conditions does not produce any such 90 km feature in CO_2 VMR (artifacts or as an instability) for many different starting conditions varying the SZA, atomic O and $O(^1D)$ VMR profiles. Couple of examples have been already shown in Figs. 13 and 12, which shows that the retrieval is capable of retrieving the "strangely" shaped CO_2 VMR profile, somewhat smaller peak (such CO_2 VMR profile was taken from one of the real inversions). Our tests confirm that the 90 km peak is going to be retrieved without problem (as this region is not strongly optically thick) if it is in fact present. With this high degree of confidence in the retrieval method, other causes were investigated, as discussed below.

An attempt was made to explain this behavior as a by-product of uncertain (unretrieved) parameters (O, $O(^1D)$, N_2, pressure, etc). Different altitude variations have been imposed in these atmospheric variables, as well as scaling of the VMRs. However, every synthetic retrieval yielded a negative result as far as reproducing the 90 km CO_2 VMR feature. Then, we tested potential biases in non-LTE parameters, however, it was also demonstrated that the non-LTE parameters do not impose this kind of vertical structure on the CO_2 VMR. The contamination of Ch7 with NO^+ emissions, which as shown in Mertens et al. (2009), increase with increasing altitudes and contribute little at 90 km and cannot produce a localized peak. As discussed above, the largest biases coming from the non-LTE retrieval processes are around 70 km, but none with a sharp peaking "knee" at the 90 km altitude as illustrated in Fig. 15. A number of numerical experiments were performed to investigate possible instrumental effects including that of mischaracterization of the FOV and its far wings. First, we attempted to correlate the observed peaks with SZA, polar summer cloud occurrences, space-craft beta angle as a function of time, latitude and longitude, looking for pattern which could provide a clue, but we did not find any consistent correlations. Then, a number of numerical experiments were performed with forward radiance profiles calculated from inputs where convolved with different FOVs in order to find what kind of FOV is needed to produce the radiance ratios similar to those shown in Fig. 16. Nevertheless, all of these attempts were inconclusive. We have also simulated an "unknown" physical processes on the 4.3 μm radiation; i.e., what kind of vertical profile is required in extra pumping of either 4.3 μm FB, FH and/or SH bands to reproduce the 90 km CO_2 VMR

Fig. 16. Ch7 radiance ratios (measured/calculated) at the first iteration in the inversion where the WACCM CO_2 VMR is taken as the initial profile. This distribution is plotted for a day 2003, 196 between latitudes 65–83°N. The individual profiles are shown as gray dotted curves, and the black curve shows the mean.

peak in synthetic retrievals. This was accomplished by introducing an artificial V–T (pumping only) term with various altitude profiles. Experiments perturbing the source function directly were also done. Nevertheless, we could not reproduce the exact shape of the observed peak, without introducing additional biases at other altitudes not seen in real retrievals. In connection with these test we also ruled out daytime OH pumping of CO_2 bands, since daytime OH is too low in number density and peak at different altitude to account for the extra 5–40% enhancement of the signal in Ch7 at around 90 km. In close collaboration with GATS Inc., responsible for SABER signal calibration, we reviewed the absolute gain calibrations and concluded that this uncertainty also cannot cause the observed CO_2 peak in the polar summer.

While it is clear that these CO_2 VMR profile features peaking around 90 km are incompatible with the current understanding of the $CO_2(\nu_3)$ emission formation, there is still a possibility that some yet to be discovered mechanism is responsible. The MLT region 85–95 km is known for various layered phenomena such as a metallic and meteoric dust layer, which one may speculate to play some role in producing the 4.3 μm enhancement of radiance. It turns out that SABER might not be the only limb emission experiment, which yields such vertical profiles. The CRISTA experiment inversions for CO_2 density (Kaufmann et al., 2002) performed with the forward fitting algorithm described by Gusev (2002) also showed profiles exhibiting similar features (A. Kutepov, 2010, private comm.). The 4.3 μm spectral measurements of the MIPAS instruments can be in some cases (where the measurement extend to upper MLT) also used to obtain CO_2 VMR up to the lower thermosphere, and the preliminary analysis done by the authors hints that the enhancements centered around the 90 km are present there as well to some degree, even though the analysis was performed only with a single profile in the polar summer. Furthermore, in the work on the nighttime 4.3 μm SABER emissions López-Puertas et al. (2004) report a persistent 90 km radiance enhancement that could not be explained even with a detailed modeling of the OH contributions. An OH–N_2 excitation strength increased by at least a factor of 3 was needed to bring the calculation closer to the measured values, which cannot be theoretically justified. Nevertheless, formulating a hypothesis on the physical mechanism that would increase the emissions at the 90 km altitude is beyond the scope of this work. It is brought to the attention of the scientific community for a future analysis.

Considering this feature is incompatible with any currently known physical or dynamical process responsible for establishing the polar summer CO_2 VMR profile, and neither arising due to the forward model nor the inverse process, it was deemed "unphysical" and the following constraint was included in the inversion algorithm for application to the measurements. First, the code checks whether the 90 km peak is developing along with the usually associated minima around the 77 km height. If both conditions are true for the currently retrieved profile at these altitude regions and the deviations (peak and minima) exceed 15% of the CO_2 VMR value below the retrieval grid (i.e. 65 km), then the three VMR values at (65, 77, 90) km are averaged and put at the 77 km grid point. Subsequently a line is fitted through these three values and smoothly joined to the rest of the profile by applying a 5 km wide box-car smoothing. This constraint is applied once if the conditions are met, and then the relaxation iteration continues normally until convergence or until such conditions occur again during the inversion iteration. The philosophy of this constraint is to utilize the available information in order to obtain a mean CO_2 VMR value that is still consistent with the measurement at the cost of degrading the vertical resolution. Retrieving an average of values is firmly established in inverse theory, perhaps more elegantly expressed in the framework of a priori covariance matrices and correlation lengths supplied to the Optimal Estimation approach

(Rodgers, 2000), or, in case of linear inverse theory introducing a penalizing function in normal equations by imposing a flatness of solution or its departure from some mean value (Twomey, 2002). Since we apply a physical forward fitting algorithm the smoothing and/or averaging has to be done explicitly, as we described. A few other constraints were conceived and tested, such as fitting different higher order polynomials. However, the polynomial fits were found to introduce solutions that showed unphysical altitude, latitude and time variability when applied to measurements from different years. Under polar summer conditions above 90 km altitude the relaxation continues without difficulties, therefore, without any additional constraints. In addition we should note that there is no strict, "z=90 km", condition in applying these constraints. The constraints are applied depending on where the CO_2 VMR peak develops during the inversion in the polar summer, which ranges from 85 to 94 km with mean typically around 90 km. It should be also stressed that it is only in the polar summer conditions that the CO_2 VMR profile is constrained below 90 km, for other seasons and/or latitudes the inversion proceeds unconstrained down to the lower boundary. The temperature relaxation is always performed with the currently obtained CO_2 VMR profile during the global iteration with or without the applied constraint. An example of the retrieved profiles from the SABER measurements subjected to the constraints described above at hight summer latitudes is shown (for the month of June) in Fig. 18, showing both high, and (mid and low) latitude, which are free of the constraints. All the profiles above ~90 km are free of any a priori constraints on the shape of the profile.

The above described process constraining the majority of the polar summer profiles leads to an empirical adjustment of the temperature and CO_2 uncertainties. In addition a decision was made to limit the maximum deviations of the CO_2 VMR errors near the bottom boundary (65–70 km) due to the retrieved $O(^1D)$ VMR uncertainties, which have typical error vertical profiles as shown in Figs. 14 and 15. The reason is two-fold. First, the WACCM and retrieved CO_2 is smoothly joined at the 65 km. Second, there is no seasonal and/or spatial pattern to these errors and the errors are manifested either as an enhancement or a depletion "knee" peaking below 70 km. We have thoroughly investigated a possible seasonal and/or spatial pattern of this feature to perhaps better determine systematic biases in the $O(^1D)$ VMR and/or to adjust the
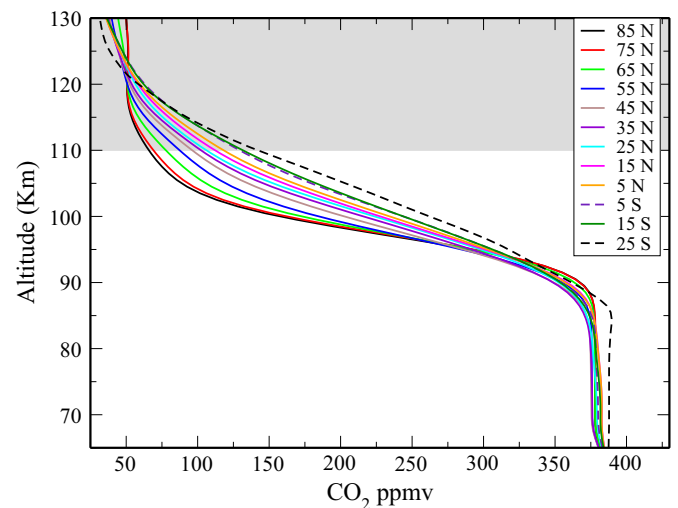

Fig. 18. Zonal monthly mean profiles of the retrieved CO_2 VMR at various latitudes for the month of June. The latitude bin is $\pm 10°$. Shaded region above 110 km indicates a region where the 2-channel inversion no longer proceeds self-consistently and the retrieved CO_2 VMR relies on the inputs takes from the WACCM model for $T_k(p)$, O, and $O(^1D)$.

Table 3
Single profile retrieval errors in the two-channel retrieved kinetic temperature and CO_2 VMR with implemented constraint.

	Altitude (km)	
	70 km	80 km
Root-Sum-Squared T_k (K)	4	4
Root-Sum-Squared CO_2 (%)	15	15

Fig. 19. Zonal monthly mean profiles of the retrieved CO_2 VMR at various latitudes for the month of March. The latitude bin is $\pm 10°$. Shaded region above 110 km indicates a region where the 2-channel inversion no longer proceeds self-consistently and the retrieved CO_2 VMR relies on the inputs takes from the WACCM model for $T_k(p)$, O, and O(^{1}D).

related non-LTE rate coefficients. However, there was no strong spatial and/or temporal pattern found. Therefore, the CO_2 errors starting at 70 km are damped not to exceed 15% of the constant values for a given profile. Such constraints yield smaller uncertainty values in the retrieved CO_2 VMR, which also impacts the T_k uncertainty below 80 km as given in Table 3. Above the 90 km altitude the 2-channel relaxation is free of any constraints and the error assessment should be taken as given in Tables 1 and 2.

The vertical resolution of the retrieved profiles varies as a function of altitude, but indirectly also from profile to profile as a function of time. This is due to the smoothing applied during the relaxation inversion, which in turn depends on external conditions as previously discussed. The non-LTE effects may also contribute considerably to the smoothing of the retrieved profiles, especially the CO_2 VMR below 80 km. In addition, it is the actual temperature profile which determines how the non-LTE effects will be manifested in the 15 μm channel. This exacerbates the problem of determining profile-to-profile vertical resolution estimates. However, because of the large self-consistency study performed with a number of temperature profiles of various vertical structures and amplitudes we can provide reliable estimates on the *best*, *worst*, and "*typical*" achievable vertical resolution.

Depending on how many iterations the inversion takes the T_k profile vertical resolution may vary between 2 and 6 km. This estimate has been validated a posteriori by comparing vertical features of the temperature profile obtained from the current SABER operational processing and the 2-channel inversion T_k profile. This is understandable as only a 2 km boxcar averaging is applied in succession every 4 iterations. Therefore, all the major fine vertical features are preserved even though the amplitudes may be reduced if the relaxation continues for entire 14 global iterations. We find that it takes longer to converge for cold polar summer mesopause conditions.

Similarly, we estimate that the retrieved CO_2 VMR vertical resolution will vary between 4 and 12 km, depending on the season and altitude (degraded resolution due to non-LTE effects below 80 km). A better resolution is generally achieved during fall/spring seasons (at all altitudes), where the convergence is faster. It can be argued that the $CO_2(z)$ should be a smooth function and even for the typical vertical resolution of 8 km no physically meaningful features should be missed. Also, as discussed previously, in the polar summer hemisphere only a mean value of CO_2 VMR is derived for altitudes below the peak (90 km).

6. First results

The prime objective of this work was to develop a self-consistent two channel inversion of the broad-band SABER Ch1 and Ch7 radiance profiles in the MLT region for the $T_k(p)$ and CO_2 VMR. The profiles obtained with this algorithm should add to better characterization of the spatial and temporal variability of radiative and dynamical processes in the MLT region. The global coverage and the long-term data availability promises that seasonal and trend studies can be differentiated at different latitudes. The entire 13-plus years of SABER data have been processed with this new
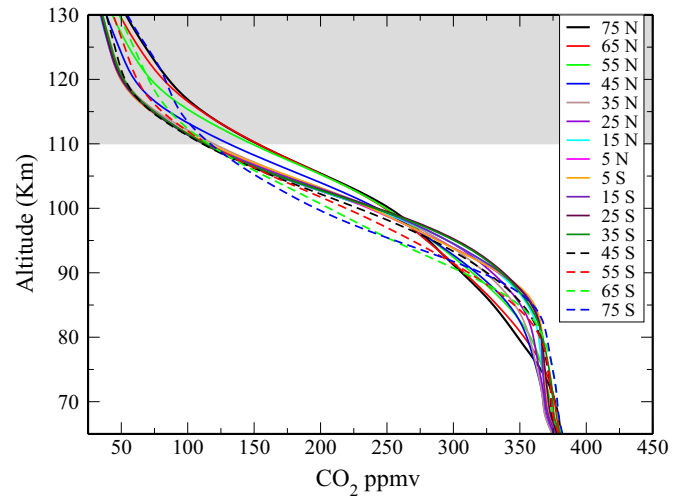
algorithm and are available to the scientific community. Here we present the most significant features of the derived CO_2 VMR profiles to summarize the new product. Mean CO_2 profiles for different latitudes (for 2012) are shown in Fig. 18 for the month of June and for March in Fig. 19. In the case of June, the latitudinal distribution of the CO_2 VMR profiles shows significant variability above 90 km where the nearly constant volume mixing ratio starts to decrease sharply with altitude. The negative slope is strongest at polar summer latitudes, however, these profiles also exhibit nearly constant VMR with altitude above 115 km. In some cases even slightly increasing values with altitude may be present starting around 125 km altitude, which may or may not be a result of uncertain O(^{1}D) VMR profile. At low latitudes, especially in the winter hemisphere, the CO_2 profiles show a constant slope from 90 to 120 km, which is a general feature of the profiles. The equinox CO_2 VMR profiles (Fig. 19) have qualitatively different behavior. In the northern hemisphere high latitudes in March the CO_2 VMR profile departs from the well mixed value below 70 km. This is the lowest altitude of departure from the constant VMR value for any season. The slope is the steepest between 70 and 100 km altitude where the CO_2 profile reaches the highest absolute value of the VMR and afterward it falls off more gradually above that height. In general, the equinox mean CO_2 profiles have a negative gradient starting at quite low altitudes (70 km) although the slope is decreasing with decreasing latitude. At the equator the profile shows nearly well mixed values up to 83–87 km but such profiles tend to have the lowest thermospheric VMR values. At the high latitudes in southern hemisphere, the CO_2 profiles do not have a constant VMR in the mesosphere, but a small negative gradient is present. Then at 85 km the decrease is more rapid again up to altitudes around 100 km above which the decrease becomes again more gradual. Detailed comparison and discussion of the retrieved CO_2 VMR and comparisons with the WACCM model and ACE-FTS profiles is presented in Rezac et al. (2014).

The temperature fields obtained from the simultaneous 2-channel retrieval, qualitatively speaking, do not deviate strongly from the SABER operational algorithm which uses a WACCM CO_2 VMR. In general, the largest absolute value differences occur in the upper MLT, especially near the polar summer latitudes. This is mostly a direct result of the differences between the retrieved CO_2 VMR and the WACCM profiles. Fig. 20 shows latitude distribution
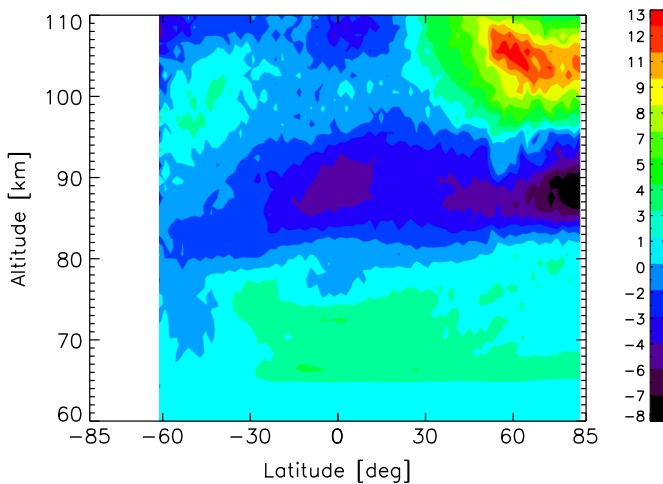
Fig. 20. Altitude latitude cross-section of difference between 2-channel and SABER operationally retrieved kinetic temperature. This example is for the month of May, 2012. The color bar values are in units of degrees Kelvin. (For interpretation of the references to color in this figure caption, the reader is referred to the web version of this paper.)

of temperature differences between the newly retrieved and the SABER operational T_k for May, 2012. Below the mesopause (65–80 km) the simultaneously obtained T_k is between 0 and 3 K warmer, while around 83–93 km region (mesopause at high latitudes) it is colder by 4–5 K, with the largest difference of 9–10 K occurring in the high latitudes of the northern (spring) hemisphere. It should be noted that in the region 65–80 km the temperature differences are usually within the total retrieval uncertainties. Nevertheless, there might be effects other than the differences in CO_2 VMR that may contribute to the small but systematic T_k offsets. A combination of the following processes could be responsible: joining of the retrieved 2-channel temperature with the profile below. A possibility of a residual effect coming from operational SABER T_k retrieval, where LTE and non-LTE inversions are merged in this region. Another effect due to hydrostatic adjustment of pressure may locally be perturbed going through this region (i.e., lower boundary of the 2-channel inversion). In general, the simultaneous $T_k(p)/CO_2$ retrieved temperatures in the lower thermosphere (100–110 km) in summer are warmer by about 5–10 K with maximum deviation of up to 15 K. This pattern is present for latitudes starting at latitude 30–35° and extending toward the summer pole.
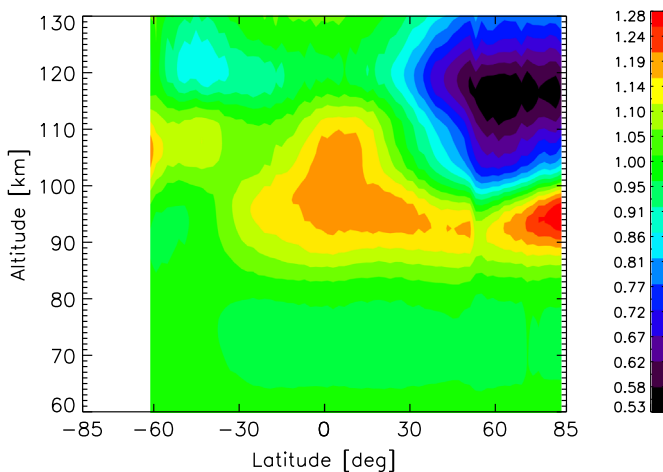

Fig. 21. Altitude latitude cross-section of ratios between CO_2 VMR retrieved from SABER in this work to the WACCM profile taken as a first guess. This example is for the month of May, 2012.

The corresponding plot of ratios of the CO_2 retrieved to the WACMM (initial profile) is shown in Fig. 21. This is complementary to the temperature distribution shown in Fig. 20, and shows the latitude distribution of the retrieved CO_2 relative to WACCM. It should be kept in mind that above 110 km the CO_2 inversion relies predominantly on the WACCM inputs, including the temperature. It is visible from this figure that retrieved CO_2 in high latitudes is well mixed up to 90–95 km, but then rapidly decreases above these altitudes with VMR significantly smaller than WACCM (the profiles look basically as shown in Fig. 18). There is also a sudden "jump" in the ratios around latitude 52–53°N, which is associated with the surface pressure jump due to change in the mean local solar time conditions at this latitude as shown in Fig. 1.

7. Summary and discussion

The SABER experiment has already returned significant scientific results during its 13 years of operations. The nearly global coverage of the data has yielded new knowledge on the spatial and temporal variability of dynamics, energetics and composition. The operationally retrieved parameters (T_k, O_3, and several volume emission rates) are routinely used in dynamical and trend studies e.g. Gao et al. (2010), Xu et al. (2013), Smith et al. (2013), Goldberg et al. (2013). The absolute values of the T_k profiles are not crucial in these cases; only its precision is important.

In this paper we have presented a self-consistent method for a two-channel non-linear retrieval of the T_k/CO_2 VMR from broadband measurements of non-LTE emissions at 15 and 4.3 μm. The method was developed and applied to daytime limb emissions measured by the SABER instrument. The entire 13-plus years of SABER data have been processed with this new algorithm and are available for access by the scientific community. The CO_2 non-LTE ro-vibrational populations were calculated using the ALI-ARMS package. The limb radiance calculations employed the LBL technique, thereby accurately accounting for overlap between lines of the same and other bands. Spectral overlap effects on the integrated limb radiance larger than 1% are noticeable at altitudes up to 85–90 km in Ch7. Sensitivity investigations of the major error mechanisms that influence the retrieved parameters were presented and demonstrate that results are consistent and of good quality.

With the new, self-consistently produced T_k/CO_2 it may be that some of the temperature differences in the mesosphere between SABER and other instruments (Sheese et al., 2012; Christensen et al., 2013) will be reduced, although this is a subject of the future work as part of validation activity of the atmospheric products derived from the 2-channel approach.

The simultaneously retrieved temperatures are usually colder in the summer hemisphere mid- and high-latitudes, where the retrieved CO_2 VMR profile has a nearly well mixed value up to higher altitudes than the WACCM model. The general seasonal behavior of the retrieved CO_2 VMR is consistent with the general circulation pattern of up-welling and increased eddy mixing in the summer hemisphere and down-welling in southern hemisphere. During equinoxes a clear transition phase is seen in the latitudinal distribution of the CO_2 VMR between the hemispheres. A detailed validation and comparison of the self-consistently retrieved T_k/CO_2 from SABER to model results as well as other instruments is presented in the paper Rezac et al. (2014).

The main conclusions regarding the self-consistency, sensitivity and error analysis of the two-channel algorithm are as follows:

- Significant coupling exists between the SABER 15 and 4.3 μm channels, which strongly increases the ill-posed nature of the inversion. The inter-dependence of the channels sets a limit on the lowest altitude boundary for the retrieval at above 50–55 km, but set to 65 km in this work to avoid problems. The

high optical thickness of the 4.3 μm bands in the region 70–75 km leads to noticeable (inverse) sensitivity in the limb radiances to the local kinetic temperature perturbation, which is due to opacity redistribution among the CO_2 bands. Another coupling mechanism is the hydrostatic equilibrium, which links these channels also as a function of altitude, and adds to the non-linearity of the inverse problem. As discussed, the temperature dependence of the collisional rate coefficients also reflects in the coupling of the channels during inversion. This is the first time the 15 and 4.3 μm channel coupling mechanisms were identified and specifically studied in the context of 2-channel inversion.

- These results bear significance for designing future space instruments relying on these two spectral regions of CO_2 molecular emissions for temperature and CO_2 retrievals. The potential future instrument should carefully consider, which spectral regions (broad-band channel) to select taking into account/avoiding the coupling of the bands as discussed.

- Retrievals using synthetic radiances show that reasonable starting conditions (within global shifts of $\pm 20\%$ on the CO_2 VMR and ± 15 K in T_k) allow a stable two-channel retrieval in a self-consistent fashion. The two-channel algorithm is demonstrated to accurately obtain T_k and/or CO_2 VMR profiles starting with a variety of initial conditions including "wave" perturbations, significant CO_2 structure, and including the cold polar summer conditions. The studies further revealed that the retrieved profiles are nearly independent of the starting CO_2 VMR distribution, but do have some dependence on the starting T_k profile, which turns out to be a dependence on the different pressure profiles via hydrostatic equilibrium.

- A large optical thickness in the 4.3 μm channel around 73–75 km and 110 km leads to strong sensitivity of the 2-channel retrieved CO_2 VMR to several atmospheric parameters as well as non-LTE parameters. In particular, large CO_2 VMR uncertainties result from the collisional rates associated with the $O(^1D) \rightarrow N_2$ energy transfer and subsequently from the $N_2 \leftrightarrow CO_2$ V–V energy exchange. In addition, below 70 km a large contribution to the error budget may come from the uncertainty in the V–T splitting rate of the $CO_2(\nu_3)$ quanta into 1–4 $CO_2(\nu_2)$ quanta during collisions with N_2 or O_2.

- We have made an estimate of additional uncertainty on the retrieved parameters from the assumption of horizontal homogeneity of the atmosphere. A posteriori statistical analysis of the entire (13+ years) SABER dataset of retrieved T_k/CO_2 showed that additional RMS error of ± 4 K on temperature and 5 ppmv on CO_2 may be incurred (at all altitudes considered). This estimate includes effects of horizontal inhomogeneity of atomic O, and $O(^1D)$ and their influence on the retrieved T_k/CO_2 in the altitude region where the O and $O(^1D)$ are retrieved, while only model (WACCM) variability is taken implicitly into account above. This error estimates should be viewed only as an upper limit, since we cannot entirely decouple temporal variability versus horizontal inhomogeneity in this approach. Due to this fact, we do not explicitly include in total retrieval error. Rigorous study of this effect is desired in the future work.

- The total uncertainty in the unconstrained CO_2 VMR retrieval reaches 35% at 70 km, decreases to 12% at 90 km and gradually increases to 32% at 110 km where the $O(^1D)$ sensitivity peaks. At the upper boundary (130 km) the uncertainty decays again to 22%. The T_k uncertainty is strongly influenced by the error in the CO_2 VMR at 70 km and to a certain degree also at 110 km (30 K). Above 90 km the T_k is sensitive to the uncertainty of the V–T rate coefficient for the $CO_2 + O$ reaction and/or the atomic O VMR uncertainty.

- In the application of the algorithm to the v2.0 SABER measurements a persistent feature appears in the CO_2 VMR profile

for the majority of the polar summer cases. A sharp enhancement centered in the region 87–94 km, with subsequent depletion below reaching a minimum at 77 km. The minimum at 77 km is not present in 100% of cases, and may change to maximum for certain periods and latitude bands. This feature remains unexplained within the realm of known physics of the non-LTE emission, and physical/dynamical processes governing the vertical CO_2 profile. A number of possible hypotheses were investigated in order to find the explanation, but so far none have provided a comprehensive resolution to this problem. There still exists a possibility that this feature may be a result of yet unknown physical processes forming the Ch7 radiance, such as collisional pumping of the ν_3 levels by supra-thermal neutral or ions. However, a concrete hypothesis has not yet been postulated. We bring this problem to light, but leave it to separate investigations in the future. For the current data version, we apply a "dynamical" (condition based) constraint to the polar summer CO_2 VMR profiles below where the 90 km feature develops as detailed in Section 5.5. The aim is to provide a mean CO_2 value in this region as constrained by the SABER measurements. The RMS difference between measured and calculated radiances is significantly smaller for this constrained profile than the initial WACCM CO_2 VMR profile, therefore we conclude that SABER measurements suggest CO_2 VMR being well mixed up to higher altitudes toward the high latitude summer hemisphere.

- Due to a smooth transition into the WACCM constant VMR profiles in the transition region at 65 km and below, a conditional damping is imposed on the maximum deviation that the CO_2 VMR can reach below the 70 km altitude fixed at 15% of the constant value. This leads to an adjusted uncertainty on the CO_2 VMR below the 80 km as given in Table 3. This also slightly improves the T_k uncertainties in this region, since CO_2 VMR is not allowed to depart from the well mixed value below (60 km) taken from the WACCM. This range of uncertainties is expected in the SABER two-channel retrieved T_k/CO_2 from SABER below 90 km. Above the 90 km altitude, the relaxation algorithm proceeds without any additional constraints for all latitudes and seasons. Above 125–130 km the CO_2 retrieved is smoothly joined into the WACCM CO_2 VMR profile.

This paper was aimed to describe the 2-channel inversion approach, its performance and the error analysis arising from various sources. The entire 13+ years of SABER daytime dataset have been processed and below we summarize the major qualitative features of the SABER v2.0 retrieved CO_2 VMR and temperature. The main characteristics as well as seasonal and latitudinal behavior of these profiles can be summarized as follows:

- The retrieved CO_2 VMR profile (as global mean) appears to be well mixed up to 80–85 km, however, the altitude where the onset of the strong CO_2 VMR decay occurs depends on latitude and season. At the high latitudes ($\pm 65°$) during equinox conditions, the CO_2 VMR profiles start to decay from the well mixed value as low as 65–70 km, and the CO_2 VMR values are usually a few percent smaller than the WACCM VMR.

- The retrieved CO_2 VMR profiles suggest inter-hemispheric differences that are seasonally symmetric. From Fig. 18 we see that CO_2 VMR has considerable latitude variations at all altitudes, especially in the thermosphere. The same pattern is observed, for example, in December (figure not shown) with polar summer occurring in the southern hemisphere. This symmetry is routinely observed in the SABER CO_2 VMR. More detailed comparisons are provided in Rezac et al. (2014).

- The two-channel retrieved temperatures exhibit very similar spatial variability compared to the SABER operationally retrieved T_k (Fig. 20), but are generally colder in the broader region around mesopause, especially in the polar summer

hemisphere by 5–12 K, as a result of higher CO_2 retrieved. An exception to the generally colder temperature profiles is the high latitudes during the equinox seasons.

Appendix A. Abbreviations used in the text

ALI-ARMS: accelerated lambda iterations for atmospheric radiation and molecular spectra

CRISTA: CRyogenic Infrared Spectrometers and Telescopes for the Atmosphere

DFE: discontinuous finite element

FOV: field of view

GCM: General Circulation Model

HITRAN: HIgh-resolution TRANsmission molecular absorption database

LOS: line of sight

LTE: local thermodynamic equilibrium

MLT: mesosphere and lower thermosphere

NER: noise equivalent radiance

ODF: opacity distribution functions

RMS: root mean square

SABER: Sounding of the Atmosphere using Broadband Emission Radiometry

S/N: signal to noise ratio

SZA: solar zenith angle

TOA: top of the atmosphere

TIMED: Thermosphere Ionosphere Mesosphere Energetics and Dynamics

VMR: volume mixing ratio

WACCM: Whole Atmosphere Community Climate Model

References

Akmaev, R.A., 2002. Modeling the cooling due to CO_2 increases in the mesosphere and lower thermosphere. Phys. Chem. Earth 27, 521–528.

Beagly, S.R., Boone, C.D., Fomichev, V.I., Jin, J.J., Semeniuk, K., McConnell, J.C.,

Bernath, P.F., 2010. First multi-year occultation observations of CO_2 in the MLT by ACE satellite: observations and analysis using the extended CMAM. Atmos. Chem. Phys. 10, 1133–1153.

Bischof, W., et al., 1985. Increased concentration and vertical distribution of carbon dioxide in the stratosphere. Nature 316, 708–710.

Carlotti, M., 1988. Global-fit approach to the analysis of limb-scanning atmospheric measurements. Appl. Opt. 27, 3250–3254.

Castor, J.I., Dykema, P.G., Klein, R.I., 1992. A new scheme for multidimensional line transfer, part II. J. Astrophys. 387, 561–571.

Chahine, M.T., 1972. A general relaxation method for inverse solution of full radiative transfer equation. J. Atmos. Sci. 29, 513–518.

Christensen, A.B., Bishop, R.L., Budzien, S.A., Hecht, J.H., Mlynczak, M.G., Russell, J. M., Stephan, A.W., Walterscheid, R.W., 2013. Altitude profiles of lower thermospheric temperature from RAIDS/NIRS and TIMED/SABER remote sensing experiments. J. Geophys. Res. (Space Phys.) 118, 3740–3746. http://dx.doi.org/10.1002/jgra.50317.

Edwards, D.P., López-Puertas, M., Lopez-Valverde, M.A., 1993. Non-local thermodynamic equilibrium studies of the 15 μm bands of CO_2 for atmospheric remote sensing. J. Geophys. Res. 98, 14955–14977.

Feofilov, A.G., Kutepov, A.A., 2012. Infrared radiation in the mesosphere and lower thermosphere: energetic effects and remote sensing. Surv. Geophys. 33, 1231–1280. http://dx.doi.org/10.1007/s10712-012-9204-0.

Feofilov, A.G., Kutepov, A.A., Pesnell, W.D., Goldberg, R.A., Marshall, B.T., Gordley, L. L., García-Comas, M., López-Puertas, M., Manuilova, R.O., Yankovsky, V.A., Petelina, S.V., Russell III, J.M., 2009. Daytime SABER/TIMED observations of water vapor in the mesosphere: retrieval approach and first results. Atmos. Chem. Phys. Discuss. 9, 13943–13997.

Feofilov, A.G., Kutepov, A.A., She, C., Smith, A.K., Pesnell, W.D., Goldberg, R.A., 2012. $CO_2(\nu_2)$-O quenching rate coefficient derived from coincidental SABER/TIMED and Fort Collins lidar observations of the mesosphere and lower thermosphere. Atmos. Chem. Phys. 12, 9013–9023.

Gao, H., Xu, J., Wu, Q., 2010. Seasonal and QBO variations in the OH nightglow emission observed by TIMED/SABER. J. Geophys. Res. (Space Phys.) 115, 6313. http://dx.doi.org/10.1029/2009JA014641.

Garcia, R.R., Manuel, L.P., Funke, B., Marsh, D.R., Kinnison, D.E., Smith, A.K., González-Galindo, F., 2014. On the distribution of CO_2 and CO in the mesosphere and lower thermosphere. J. Geophys. Res. 119 (9), 5700–5718.

García-Comas, M., López-Puertas, M., Marshall, B.T., Wintersteiner, P.P., Funke, B., Bermejo-Pantaleón, D., Mertens, C.J., Remsberg, E.E., Gordley, L.L., Mlynczak, M. G., Russell III, J.M., 2008. Error in sounding of the atmosphere using broadband emission radiometry (SABER) kinetic temperature caused by non-local thermodynamic equilibrium model parameters. J. Geophys. Res. 113.

Girard, A., Besson, J., Brard, D., Laurent, J., Lemaitre, M.P., Lippens, C., Muller, C., Vercheval, J., Ackerman, M., 1988. Global results of Grille spectrometer experiment on board of Spacelab 1. Planet. Space Sci. 36, 291–300.

Goldberg, R.A., Feofilov, A.G., Pesnell, W.D., Kutepov, A.A., 2013. Inter-hemispheric coupling during northern polar summer periods of 2002–2010 using TIMED/SABER measurements. J. Atmos. Sol.-Terr. Phys. 104, 277–284. http://dx.doi.org/10.1016/j.jastp.2012.11.018.

Gusev, O., 2002. Non-LTE Diagnostics of the Infrared Observations of the Planetary Atmosphere (Ph.D. thesis). Ludwig-Maximilians University, Munchen.

Gusev, O.A., Kaufmann, M., Grossmann, K.U., Schmidlin, F.J., Shepherd, M.G., 2006. Atmospheric neutral temperature distribution at the mesopause altitude. J. Atmos. Sol.-Terr. Phys. 68, 1684–1697.

Gusev, O.A., Kutepov, A.A., 2003. Non-LTE gas in planetary atmospheres. In: ASP Conference Series, vol. 228, pp. 318–230.

Harris, R.D., Adams, G.W., 1983. Where does the $O(^1D)$ energy go? J. Geophys. Res. 88, 4918–4928.

Hubeny, I., Lanz, T., 1995. Non-LTE line-blanketed model atmospheres of hot stars. 1: hybrid complete linearization/accelerated lambda iteration method. Astrophys. J. 439, 875–904. http://dx.doi.org/10.1086/175226.

Kaufmann, M., Gusev, O.A., Grossmann, K.U., Roble, R.G., Hagan, M.E., Hartsough, C., Kutepov, A.A., 2002. The vertical and horizontal distribution of CO_2 densities in the upper mesosphere and lower thermosphere as measured by CRISTA. J. Geophys. Res. 107. http://dx.doi.org/10.1029/2001JD000704.

Kaufmann, M., Zhu, Y., Ern, M., Riese, M., 2014. Global distribution of atomic oxygen in the mesopause region as derived from SCIAMACHY O(1S) green line measurements. Geophys. Res. Lett. 41, 6274–6280. http://dx.doi.org/10.1002/2014GL060574.

Kurucz, R.L., 1995. The solar irradiance by computation. In: Anderson, G.P., Picard, R. H., Chetwynd, J.H. (Eds.), Proceedings of the 17th Annual Conference on Atmospheric Transmission Models. Hanscom Air Force Base, MA, pp. 333–334.

Kutepov, A.A., Feofilov, A.G., Marshall, B.T., Gordley, L.L., Pesnell, W.D., Goldberg, R. A., 2006. SABER temperature observations in the summer polar mesosphere and lower thermosphere: importance of accounting for the CO_2 ν_2 quanta V–V exchange. Geophys. Res. Lett. 33. http://dx.doi.org/10.1029/2006GL026591.

Kutepov, A.A., Gusev, O.A., Ogibalov, V.P., 1998. Solution of the non-LTE problem for molecular gas in planetary atmospheres: superiority of accelerated lambda iteration. J. Quant. Spectrosc. Radiat. Transf. 60, 199–220.

Lindzen, R.S., 2007. Taking greenhouse warming seriously. Energy Environ. 18, 936–950.

López-Puertas, M., García-Comas, M., Funke, B., Picard, R.H., Winick, J.R., Wintersteiner, P.P., Mlynczak, M.G., Mertens, C.J., Russell III, J.M., Gordley, L.L., 2004. Evidence for an $OH(\nu)$ excitation mechanism of CO_2 4.3 μm nighttime emission from SABER/TIMED measurements. J. Geophys. Res. 109, D09307.

López-Puertas, M., López-Valverde, M.A., Garcia, R.R., Roble, R.G., 2000. A review of

CO_2 and CO abundances in the middle atmosphere. In: Siskind, D.E., Eckermann, S.D. , Summers M.E. (Eds.), Atmospheric Science Across the Stratopause, AGU, Washington DC, Geophysical Monograph Series, vol. 123, pp. 83–100.

López-Puertas, M., López-Valverde, M.A., Taylor, F.W., 1992. Vibrational temperatures and radiative cooling of the CO_2 15 μm bands in the middle atmosphere. Q. J. R. Meteorol. Soc. 47, 499–532.

López-Puertas, M., Taylor, F.W., 1989. Carbon Dioxide 4.3 μm emissions in the Earth's atmosphere: a comparison between NIMBUS 7 SAMS measurements and non-LTE radiative transfer calculations. J. Geophys. Res. 94, 12068–13045.

López-Puertas, M., Taylor, F.W., 2001. Non-LTE Radiative Transfer in the Atmosphere. Series on Atmospheric. Oceanic and Planetary Physics, vol. 3. World Scientific, Singapore.

López-Puertas, M., Zaragoza, G., López-Valverde, M.A., Taylor, F.J.W., 1998. Non local thermodynamic equilibrium (LTE) atmospheric limb emission at 4.6 μm. 1. An update of the CO_2 non-LTE radiative transfer model. J. Quant. Spectrosc. Radiat. Transf. 103, 8499–8513.

Marshall, B.T., Gordley, L.L., Chu, D.A., 1994. BANDPAK: algorithms for modeling broadband transmission and radiance. J. Quant. Spectrosc. Radiat. Transf. 52, 581–599.

Mertens, C.J., Mlynczak, M.G., Lopez-Puertas, M., Wintersteiner, P.P., Picard, R.H., Winick, J.R., Gordley, L.L., Russell III, J.M., 2003. Retrieval of kinetic temperature and carbon dioxide abundance from nonlocal thermodynamic equilibrium limb emission measurements made by the SABER experiment on the TIMED satellite. In: Schaefer, K.P., Lado-Bordowsky, O., Comeron, A., Picard, R.H. (Eds.), Remote Sensing of Clouds and the Atmosphere VII, pp. 162–171. http://dx.doi.org/10.1117/12.463358.

Mertens, C.J., Winick, J.R., Picard, R.H., Evans, D.S., López-Puertas, M., Wintersteiner, P.P., Xu, X., Mlynczak, M.G., Russell, J.M., 2009. Influence of solar-geomagnetic disturbances on SABER measurements of 4.3 μm emission and the retrieval of kinetic temperature and carbon dioxide. Adv. Space Res. 43, 1325–1336. http://dx.doi.org/10.1016/j.asr.2008.10.029.

Mihalas, D., 1978. Stellar Atmospheres. W H Freeman & Co, San Francisco, ISBN:0716703599.

Mlynczak, M.G., Hunt, L.A., Mast, J.C., Thomas Marshall, B., Russell, J.M., Smith, A.K., Siskind, D.E., Yee, J.H., Mertens, C.J., Martin-Torres, F.J., Thompson, R.E., Drob, D. P., Gordley, L.L., 2013. Atomic oxygen in the mesosphere and lower thermosphere derived from SABER: algorithm theoretical basis and measurement uncertainty. J. Geophys. Res. 118, 5724–5735.

Oeschger, H., Siegenthaler, U., 1987. Biosphere CO_2 emissions during the past 200 years reconstructed by deconvolution of ice core data. Tellus 39B, 140–154.

Picard, R.H., Winick, J.R., Sharma, R.D., Zachor, A.S., Espy, P.J., Harris, C.R., 1987. Interpretation of infrared measurements of the high latitude thermosphere from a rocket borne interferometer. Astron. Astrophys. 7, 1023–1030.

Remsberg, E., Lingenfelser, G., Harvey, V.L., Grose, W., Russell, J., Mlynczak, M., Gordley, L., Marshall, B.T., 2003. On the verification of the quality of SABER temperature, geopotential height, and wind fields by comparison with Met Office assimilated analyses. J. Geophys. Res. 108. http://dx.doi.org/10.1029/2003JD003720.

Remsberg, E.E., Marshall, B.T., García-Comas, M., Krueger, D., Lingenfelser, G.S., Martin-Torres, J., Mlynczak, M.G., Russell III, J.M., Smith, A.K., Zhao, Y., Brown, C., Gordley, L.L., Lopez-Gonzales, M., She, C.Y., Taylor, M.J., Thompson, R.E., 2008. Assessment of quality of the Version 1.07 temperature versus pressure profiles of the middle atmosphere from TIMED/SABER. Geophys. Res. Lett. 113, 1. http://dx.doi.org/10.1029/2008JD010013.

Rezac, L., Jian, Y., Yue, J., Russell III, J.M., Kutepov, A., Garcia, R., Walker, K., Bernath, P., 2014. Global distribution of co₂ volume mixing ratio in the mesosphere and lower thermosphere from saber. J. Geophys. Res., submitted for publication.

Rezac, L., Kutepov, A.A., Feofilov, A.G., Russell III, J.M., 2011. On limb radiance calculations and convergence of relaxation type retrieval algorithms. Appl. Opt. 50, 5499–5502. http://dx.doi.org/10.1364/AO.50.005499.

Roble, R.G., Dickinson, R.E., 1989. How will changes in carbon dioxide and methane modify the mean structure of the mesosphere and thermosphere? Geophys. Res. Lett. 16, 1441–1444.

Rodgers, C.D., 2000. Inverse Methods for Atmospheric Sounding: Theory and Practice. World Scientific, Singapore.

Rothman, L.S., Gordon, I.E., Barbe, A., Benner, D.C., Bernath, P.F., Birk, M., Boudon, V.,

Brown, L.R., Campargue, A., Champion, J., Chance, K., Coudert, L.H., Dana, V., Devi, V.M., Fally, S., Flaud, J., Gamache, R.R., Goldman, A., Jacquemart, D., Kleiner, I., Lacome, N., Lafferty, W.J., Mandin, J., Massie, S.T., Mikhailenko, S.N., Miller, C.E., Moazzen-Ahmadi, N., Naumenko, O.V., Nikitin, A.V., Orphal, J., Perevalov, V.I., Perrin, A., Predoi-Cross, A., Rinsland, C.P., Rotger, M., Simeckova, M., Smith, M.A.H., Sung, K., Tashkun, S.A., Tennyson, J., Toth, R.A., Vandaele, A.C., Auwera, J.V., 2009. The HITRAN 2008 molecular spectroscopic database. J. Quant. Spectrosc. Radiat. Transf. 110, 533–572.

Rothman, L.S., et al., 1992. The HITRAN database: editions of 1991–1992. J. Quant. Spectrosc. Radiat. Transf. 48, 469–507.

Russell III, J.M., Drayson, S.R., 1971. The inference of atmospheric ozone using satellite horizon measurements in the $1042 cm^{-1}$ band. J. Atmos. Sci. 29, 376.

Russell III, J.M., Mlynczak, M.G., Gordley, L.L., Tansock, J., Esplin, R., 1999. An overview of the SABER experiment and preliminary calibration results. Proc. SPIE Int. Soc. Opt. Eng. 3756, 277–288.

Rybicki, G.B., Hummer, D.G., 1991. An accelerated lambda iteration method for multilevel radiative transfer. I. Non-overlapping lines with background continuum. Astron. Atrophys. 245, 171–181.

Sambridge, M., Mosegaard, K., 2002. Monte Carlo methods in geophysical inverse problems. Rev. Geophys. 40. http://dx.doi.org/10.1029/2000RG000089.

Sheese, P.E., Strong, K., Llewellyn, E.J., Gattinger, R.L., Russell III, J.M., Boone, C.D., Hervig, M.E., Sica, R.J., Bandoro, J., 2012. Validation of OSIRIS mesospheric temperatures using satellite and ground-based measurements. Atmos. Meas. Tech. Discuss. 5, 5493–5526. http://dx.doi.org/10.5194/amtd-5-5493-2012.

Shved, G.M., Kutepov, A.A., Ogibalov, V.P., 1998. Non-local thermodynamic equilibrium in CO_2 in the middle atmosphere. I. Input data and populations of the ν_3 mode manifold states. J. Atmos. Sol.-Terr. Phys. 60, 289–314.

Smith, A.K., Harvey, V.L., Mlynczak, M.G., Funke, B., GarcíA-Comas, M., Hervig, M., Kaufmann, M., KyröLä, E., López-Puertas, M., McDade, I., Randall, C.E., Russell, J. M., Sheese, P.E., Shiotani, M., Skinner, W.R., Suzuki, M., Walker, K.A., 2013. Satellite observations of ozone in the upper mesosphere. J. Geophys. Res. (Atmos.) 118, 5803–5821. http://dx.doi.org/10.1002/jgrd.50445.

Stiller, G., 2002. Sensitivity of trace gas abundances retrievals from infrared limb emission spectra to simplifying approximations in radiative transfer modelling. J. Quant. Spectrosc. Radiat. Transf. 72, 249–280. http://dx.doi.org/10.1016/S0022-4073(01)00123-6.

Tamminen, J., 2004. Validation of nonlinear inverse algorithms with Markov Chain Monte Carlo method. J. Geophys. Res. 109. http://dx.doi.org/10.1029/2004JD004927.

Tans, P., Keeling, R., 2014. Trends in Atmospheric Carbon Dioxide. Downloaded from: ⟨http://www.esrl.noaa.gov/gmd/ccgg/trends/⟩.

Tarantola, A., 1987. Inverse Problem Theory, Methods for Data Fitting and Model Parameter Estimation. Elsevier Science, Philadelphia, USA.

Tarantola, A., Valette, B., 1982. Generalized nonlinear inverse problems solved using the least squares criterion. Rev. Geophys. Space Phys. 20, 219–232.

Trinks, H., Fricke, K.H., 1974. Carbon dioxide concentration in the lower thermosphere. J. Geophys. Res. 83, 3883–3886.

Trinks, H., Offermann, D., Zahn, U., Steinhauer, C., 1978. Neutral composition measurements between 90 and 220 km altitude by rocket-born mass spectrometer. J. Geophys. Res. 83, 2169–2176.

Twomey, S., 2002. Introduction to the Mathematics of Inversion in Remote Sensing and Indirect Measurements, second ed. Dower Phoenix, New York, USA.

Twomey, S., Herman, B., Rabinoff, R., 1977. An extension to the Chahine method of inverting the radiative transfer equation. J. Atmos. Sci. 34, 1085.

Winick, J.R., Picard, R.H., Sharma, R.D., Joseph, R.A., Wintersteiner, P.P., 1987. Radiative transfer effects on Aurora enhanced 4.3 μm emission. Adv. Space Res. 7, 1017–1021.

Xu, J., Smith, A.K., Wang, W., Jiang, G., Yuan, W., Gao, H., Yue, J., Funke, B., López-Puertas, M., Russell, J.M., 2013. An observational and theoretical study of the longitudinal variation in neutral temperature induced by aurora heating in the lower thermosphere. J. Geophys. Res. (Space Phys.) 118, 7410–7425. http://dx.doi.org/10.1002/2013JA019144.

Zaragoza, G., López-Puertas, M., López-Valverde, M.A., Taylor, F.W., 2000. Global distribution of CO_2 in the upper mesosphere as derived from UARS/ISAMS measurements. J. Geophys. Res. 105, 19829–19839.